Polymer stretching and alignment under the hierarchy of coherent vortices in turbulence

Yusuke Koide *

Graduate School of Engineering, Nagoya University, Furo-cho, Chikusa, Nagoya, Aichi 464-8603, Japan

Susumu Goto

Graduate School of Engineering Science, Osaka University, 1-3 Machikaneyama, Toyonaka, Osaka 560-8531, Japan

(Received 7 May 2024; accepted 6 December 2024; published 27 December 2024; corrected 21 January 2025)

We perform Brownian dynamics simulations of the finitely extensible nonlinear elastic (FENE) dumbbells in spatially periodic turbulence to investigate the relationship between the dynamics of polymers and the hierarchy of coherent vortices. We decompose the velocity field into different scales to directly evaluate the effect of vortices with different sizes on dumbbells. Scale-decomposition analysis provides quantitative evidence that the smallest-scale vortices dominantly stretch dumbbells with a relaxation time shorter than the Kolmogorov time, whereas the contribution from large-scale vortices relatively increases when the relaxation time exceeds the Kolmogorov time. To explore the origin of this scale-dependent stretching mechanism, we investigate the alignment between dumbbells and the scale-decomposed strain-rate tensor. We find that dumbbells with a shorter relaxation time than the Kolmogorov time preferentially align in the most extensional direction induced by the smallest-scale vortices. However, as the relaxation time increases, dumbbells tend to align in the most extensional direction induced by 2–4 times larger vortices than the smallest-scale vortices. We explain this relaxation-time dependence of the effect of vortices with different sizes on dumbbells by focusing on how persistently the vortices stretch dumbbells.

DOI: 10.1103/PhysRevFluids.9.123303

I. INTRODUCTION

It is well-known that small quantities of polymers can suppress turbulence [1–3]. Since turbulence causes a significant increase in friction drag, turbulence suppression by polymers has attracted practical interest. For example, it has been applied to the transport of oil [4] and firefighting [5,6]. It is widely believed that the dynamical interaction between polymers and turbulence is a key aspect of the physical mechanism of this turbulence suppression [2]. Considering that turbulence is composed of vortices with different sizes [7], as depicted in a well-known schematic of the energy cascade [8], this paper focuses on how polymers are stretched and aligned by vortices with different sizes in turbulence.

Many studies have been conducted on the dynamics and statistics of polymers in turbulent flows [9–17]. Stone and Graham [10] investigated the dynamics of polymer models in an "exact coherent state" in plane Couette flow using Brownian dynamics (BD) simulations. They showed that the bead-spring chains are significantly stretched when the Weissenberg number, defined as the product of the relaxation time and the maximum Lyapunov exponent for the velocity field (i.e., the mean

*Contact author: koide.yusuke.k1@f.mail.nagoya-u.ac.jp

stretching rate in turbulent flows), exceeds $1/2$. Watanabe and Gotoh [15] performed BD simulations of polymer models in isotropic turbulence and demonstrated that the coil-stretch (CS) transition occurs when the Weissenberg number based on the Kolmogorov time is around 3–4. Terrapon *et al.* [12] analyzed the dynamics of dumbbell models in a Newtonian turbulent channel flow, focusing on the flow topologies. They found that strong biaxial elongational flows contribute to the stretching of dumbbells in turbulence. However, they also suggested that even strong flows in turbulence cannot stretch polymers unless the flows persist enough. Hence, the timescale of turbulence fluctuations also plays an important role in the polymer dynamics. Musacchio and Vincenzi [16] examined the effect of correlation time of the velocity gradient on the statistics of the end-to-end distance of dumbbells in random flows. They revealed a scenario of the CS transition for a large Kubo number, defined as the product of the maximum Lyapunov exponent and the correlation time of the velocity gradient. In summary, previous studies on the behavior of polymers in turbulence have revealed the relevance of the strength, topology, and persistence time of turbulence.

Besides the above-mentioned characteristics of turbulence, the multiscale nature of turbulence is also an essential aspect of the interactions between polymers and turbulence. Lumley [18,19] proposed that polymers can be affected by vortices with shorter timescales than those of polymers. In contrast, Tabor and de Gennes [20] determined an upper bound on the scale of vortices capable of interacting with polymers by focusing on the energy balance. Afterward, Xi *et al.* [21] introduced the characteristic scale of vortices based on the energy flux balance. Meanwhile, the interactions between polymers and turbulence cause nontrivial energy transfer. Valente *et al.* [22] numerically demonstrated that polymers partly contribute to the energy cascade when the relaxation time is longer than the eddy turnover time. They suggested that the origin of the polymer-induced energy cascade is based on the interactions between polymers and large-scale vortices. In these ways, the multiscale feature of turbulence is closely related to the interactions between polymers and turbulence.

On the other hand, recent studies have uncovered the hierarchy of coherent vortices in Newtonian turbulence using scale-decomposition analysis to extract vortices at each scale [23]. Goto *et al.* [24] revealed the hierarchy of coherent vortices in turbulence driven by a steady force in a periodic cube by applying the bandpass filter to the velocity field. Successively, the hierarchy of coherent vortices is also confirmed in more realistic flows by applying the Gaussian filter to the velocity field, including turbulent boundary layers [25], turbulent channel flows [26], and turbulent wake flows behind a cylinder [27]. Scale-decomposition analysis has remarkably developed our understanding of the small-scale universality of turbulence. Thus, scale-decomposition analysis is also expected to shed light on how vortices with different sizes interact with polymers in turbulence.

In the present paper, we investigate the scale-dependent role of vortices in the stretching and alignment of polymers by decomposing the turbulent flows into different scales. There have been two-way coupled simulations of turbulent flows containing polymer models [28–32]. However, since the turbulent flows are significantly modified depending on the relaxation time, the maximum extension length, and the concentration of polymers, it is difficult to systematically evaluate the effect of the hierarchy of turbulence on polymer dynamics by using two-way coupled simulations. Thus, we adopt the one-way coupled method where polymer models are dissolved in Newtonian turbulent flows [10,12,15,17], corresponding to the extremely dilute limit. We aim to pave the way for understanding the physical mechanism of turbulence modulation due to polymers by quantitatively demonstrating the scale-dependent effect of vortices on the stretching and alignment of polymer models.

II. METHOD

A. Brownian dynamics simulation

We adopt the finitely extensible nonlinear elastic (FENE) dumbbell model, where the polymer molecule is considered as two beads connected by a nonlinear spring. The end-to-end vector $\boldsymbol{R}$ of

the dumbbell obeys

$$\frac{d\boldsymbol{R}}{dt} = \boldsymbol{\kappa}\cdot\boldsymbol{R} - \frac{1}{2\tau}\frac{\boldsymbol{R}}{1-R^2/R_{\max}^2} + \sqrt{\frac{4k_BT}{\zeta}}\boldsymbol{\xi}, \tag{1}$$

where $\kappa_{ij} = \partial u_i(\boldsymbol{x},t)/\partial x_j|_{\boldsymbol{x}=\boldsymbol{R}_G}$ is the velocity gradient at the position $\boldsymbol{R}_G$ of the center of mass of the dumbbell with $\boldsymbol{u}(\boldsymbol{x},t)$ being the fluid velocity, τ is the relaxation time, $R_{\max}$ is the maximum extension length, k_B is the Boltzmann constant, T is the temperature, ζ is the friction coefficient, and $\boldsymbol{\xi}$ is a random variable that satisfies

$$\langle \xi_i(t)\rangle = 0, \tag{2}$$

$$\langle \xi_i(t)\xi_j(s)\rangle = \delta_{ij}\delta(t-s), \tag{3}$$

where δ_{ij} is the Kronecker delta, $\delta(t)$ is the delta function, and $\langle\cdot\rangle$ denotes the ensemble average. Throughout this paper, we fix $R_{\max}^2$ at $3000k_BT/H$, where H is the spring constant. We have confirmed that our results remain unchanged for other $R_{\max}$, as shown in Appendix A. We assume that the thermal fluctuation has little effect on the motion of the center of mass of the dumbbell compared with the advection by turbulent flows [12,15,17]. Thus, the center-of-mass $\boldsymbol{R}_G$ of the dumbbell follows

$$\frac{d\boldsymbol{R}_G}{dt} = \boldsymbol{u}(\boldsymbol{R}_G,t). \tag{4}$$

We note that this model assumes the overdamped case, i.e., the inertial term is neglected in Eqs. (1) and (4), because the momentum relaxation is generally fast compared with the bond relaxation in polymers [33,34].

To integrate Eqs. (1) and (4), we use a semi-implicit predictor-corrector scheme [12,35] and the fourth-order Runge–Kutta–Gill scheme, respectively. The trilinear interpolation is used for $\boldsymbol{\kappa}(t)$ and $\boldsymbol{u}(\boldsymbol{R}_G,t)$ [12,15]. We set the ratio of the time step Δt_{BD} in BD simulations to the time step Δt_{DNS} in direct numerical simulations (DNSs) as 0.1 to prevent the length of dumbbells from exceeding $R_{\max}$. We use linearly interpolated $\boldsymbol{\kappa}(t)$ between $\boldsymbol{\kappa}(n\Delta t_{\mathrm{DNS}})$ and $\boldsymbol{\kappa}((n+1)\Delta t_{\mathrm{DNS}})$ obtained from DNS with $n\in\mathbb{N}$ such that $n\Delta t_{\mathrm{DNS}} \leqslant t < (n+1)\Delta t_{\mathrm{DNS}}$.

B. Direct numerical simulation

To generate Lagrangian trajectories in turbulent flows, we perform DNS of an incompressible Newtonian fluid under periodic boundary conditions in three orthogonal directions with period 2π. The three-dimensional Navier–Stokes equation with an external force $\boldsymbol{f}(\boldsymbol{x},t)$ is numerically solved using the Fourier spectral method. We use two types of external force to test the robustness of the results to the choice of forcing. The first is the steady force $\boldsymbol{f}^{(\mathrm{V})}(\boldsymbol{x})$ expressed as

$$\boldsymbol{f}^{(\mathrm{V})}(\boldsymbol{x}) = (-\sin x\cos y, \cos x\sin y, 0)^{\mathsf{T}}. \tag{5}$$

The forcing wave number k_f of $\boldsymbol{f}^{(\mathrm{V})}$ is $\sqrt{2}$. The second is the time-dependent force $\boldsymbol{f}^{(\mathrm{I})}(\boldsymbol{x},t)$ whose Fourier coefficient $\widehat{\boldsymbol{f}}^{(\mathrm{I})}(\boldsymbol{k},t)$ is expressed as

$$\widehat{\boldsymbol{f}}^{(\mathrm{I})}(\boldsymbol{k},t) = \begin{cases} \frac{P}{2E_{k_f}(t)}\widehat{\boldsymbol{u}}(\boldsymbol{k},t) & 0<|\boldsymbol{k}|\leqslant k_f \\ 0 & \text{otherwise,} \end{cases} \tag{6}$$

where P is the energy input rate, $\widehat{\boldsymbol{u}}(\boldsymbol{k},t)$ is the Fourier coefficient of $\boldsymbol{u}(\boldsymbol{x},t)$, and $E_{k_f}(t)$ is defined as

$$E_{k_f}(t) = \sum_{0<|\boldsymbol{k}|\leqslant k_f}\frac{1}{2}|\widehat{\boldsymbol{u}}(\boldsymbol{k},t)|^2. \tag{7}$$

TABLE I. Parameters and statistics of turbulence: $\boldsymbol{f}$ is the external force, N^3 is the number of Fourier modes, Re_λ is the Reynolds number based on the Taylor microscale λ, $k_{\max} = \sqrt{2}N/3$ is the largest resolved wave number, η is the Kolmogorov length, and N_t is the number of Lagrangian trajectories. The Courant–Friedrichs–Lewy (CFL) number is defined as $\sqrt{2K/3}\Delta t_\mathrm{DNS}/\Delta x$, where K is the kinetic energy per unit mass, Δt_DNS is the time step, and Δx is the grid width.

$\boldsymbol{f}$	N^3	Re_λ	$k_{\max}\eta$	CFL number	N_t
$\boldsymbol{f}^{(\mathrm{V})}$	128^3	30	2.9	6.0×10^{-2}	16^3
$\boldsymbol{f}^{(\mathrm{V})}$	512^3	120	1.7	7.0×10^{-2}	32^3
$\boldsymbol{f}^{(\mathrm{I})}$	512^3	220	1.4	5.4×10^{-2}	32^3
$\boldsymbol{f}^{(\mathrm{I})}$	1024^3	310	1.6	5.5×10^{-2}	32^3

The forcing by $\boldsymbol{f}^{(\mathrm{I})}$ leads to a constant energy input rate P [36]. We set $P = 1$ and $k_f = 2.5$. The time integration uses the fourth-order Runge–Kutta–Gill scheme, and the phase shift method removes the aliasing errors. Table I shows the DNS parameters and statistics of turbulence. In the table, N^3 is the number of Fourier modes, Re_λ is the Reynolds number based on the Taylor microscale λ, $k_{\max} = \sqrt{2}N/3$ is the largest resolved wave number, $\eta = (\nu^3/\epsilon')^{1/4}$ is the Kolmogorov length, and N_t is the number of Lagrangian trajectories, where ϵ' is the turbulent energy dissipation rate per unit mass and ν is the kinematic viscosity. Here, we define Re_λ as

$$\mathrm{Re}_\lambda = \sqrt{\frac{20}{3\nu\epsilon'}}K', \tag{8}$$

where K' is the turbulent kinetic energy per unit mass. To investigate the effect of the hierarchy of coherent vortices in turbulence, we consider four cases with different Re_λ. The Courant–Friedrichs–Lewy (CFL) number is defined as $\sqrt{2K/3}\Delta t_\mathrm{DNS}/\Delta x$, where K is the kinetic energy per unit mass and Δx is the grid width. For each trajectory, we consider $N_\mathrm{d} = 10$ dumbbells with different initial conditions and realizations of $\boldsymbol{\xi}(t)$. In what follows, to nondimensionalize τ, we use the Weissenberg number $\mathrm{Wi}_\eta = \tau/\tau_\eta$ defined as the ratio of the relaxation time τ of dumbbells to the Kolmogorov time $\tau_\eta = \sqrt{\nu/\epsilon'}$.

III. RESULTS

In this section, we identify the most influential scale of vortices in the stretching and alignment of dumbbells in turbulence using scale-decomposition analysis. Specifically, we define the velocity $\boldsymbol{u}^{(k_c)}(\boldsymbol{x}, t)$ at wave number k_c as the velocity obtained using the Fourier bandpass filter with passband $[k_c/\sqrt{2}, \sqrt{2}k_c]$ [24,37]. We have confirmed that our conclusions are insensitive to the choice of passband, as shown in Appendix B. Figure 1 shows the isosurfaces of the enstrophy $|\boldsymbol{\omega}|^2$ and the bandpass-filtered enstrophy $|\boldsymbol{\omega}^{(k_c)}|^2$ for $\mathrm{Re}_\lambda = 120$ with forcing $\boldsymbol{f}^{(\mathrm{V})}$ and $\mathrm{Re}_\lambda = 310$ with forcing $\boldsymbol{f}^{(\mathrm{I})}$. The scale decomposition with the bandpass filter extracts the hierarchy of coherent vortices with different length scales [Figs. 1(b) and 1(d)]. Otherwise, we only observe the seemingly randomized small-scale vortices [Figs. 1(a) and 1(c)]. In the following, we evaluate the scale-dependent contribution of vortices to the stretching and alignment of dumbbells using $\boldsymbol{u}^{(k_c)}(\boldsymbol{x}, t)$. Here, we describe our scale-decomposition analysis in more detail to relate the spatial filtering of the Eulerian velocity field and the Lagrangian history experienced by dumbbells. The Lagrangian velocity gradient $[\nabla\boldsymbol{u}]_L(t|\boldsymbol{x}_0, t_0)$ is determined by the Eulerian velocity gradient $\nabla\boldsymbol{u}(\boldsymbol{x}, t)$ at the instantaneous particle position $\boldsymbol{x}_L(t|\boldsymbol{x}_0)$ as follows:

$$[\nabla\boldsymbol{u}]_L(t|\boldsymbol{x}_0, t_0) = \nabla\boldsymbol{u}(\boldsymbol{x}_L(t|\boldsymbol{x}_0, t_0), t), \tag{9}$$

where t_0 is the labeling time, $\boldsymbol{x}_0$ is the position of the particle at $t = t_0$, and $\boldsymbol{x}_L(t|\boldsymbol{x}_0, t_0)$ is the position of the particle with the initial position $\boldsymbol{x}_0$ at $t = t_0$. In the present paper, $[\cdot]_L$ denotes the Lagrangian

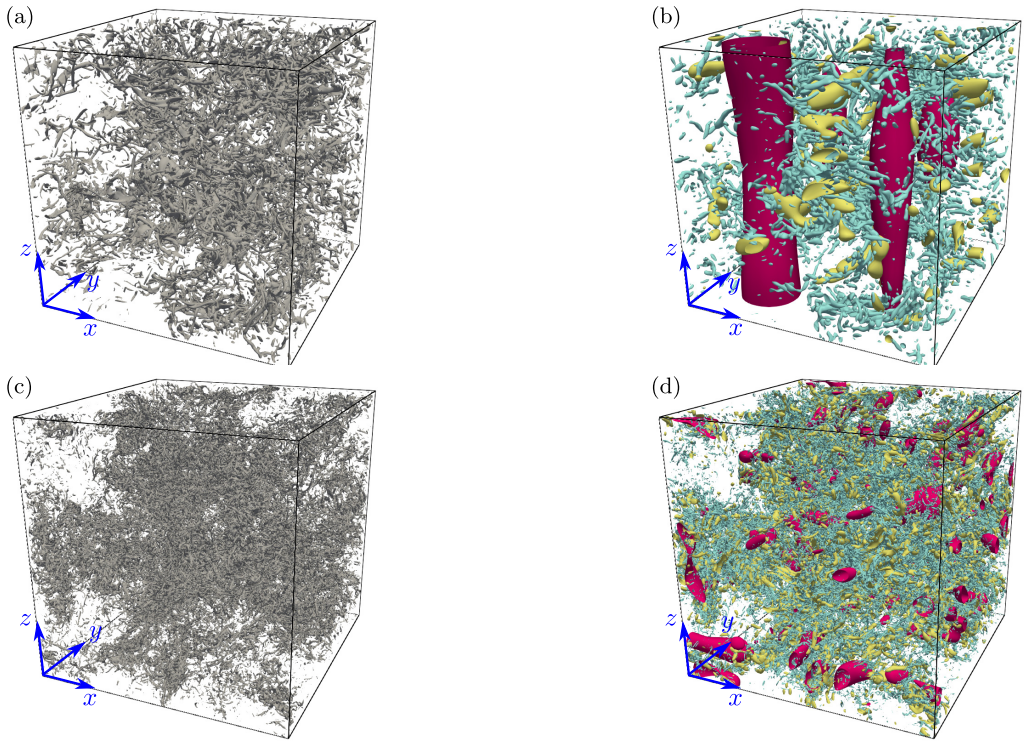

FIG. 1. Isosurfaces of [(a),(c)] raw $|\boldsymbol{\omega}|^2$ and [(b),(d)] bandpass-filtered enstrophy $|\boldsymbol{\omega}^{(k_c)}|^2$ for [(a),(b)] $\mathrm{Re}_\lambda = 120$ with forcing $\boldsymbol{f}^{(\mathrm{V})}$ and [(c),(d)] $\mathrm{Re}_\lambda = 310$ with forcing $\boldsymbol{f}^{(\mathrm{I})}$. In (b), $k_c = k_f$ (red), $4k_f$ (yellow), and $16k_f (= 0.16\eta^{-1})$ (cyan) with the forcing wave number $k_f = \sqrt{2}$. In (d), $k_c = 8\sqrt{2}k_f/5$ (red), $32\sqrt{2}k_f/5$ (yellow), and $128\sqrt{2}k_f/5 (= 0.3\eta^{-1})$ (cyan) with $k_f = 2.5$. In (a) and (c), the threshold value $\mathcal{E}$ of the isosurface is set at $\mu + 3\sigma$. In (b) and (d), $\mathcal{E}$ is set at $\mu + 3\sigma$ for the largest k_c and $\mu + 2\sigma$ for the other k_c. Here, μ and σ denote the spatial average and standard deviation of $|\boldsymbol{\omega}|^2$ and $|\boldsymbol{\omega}^{(k_c)}|^2$.

flow variable. On the other hand, the bandpass filter enables us to decompose the Eulerian velocity gradient $\nabla \boldsymbol{u}(\boldsymbol{x}, t)$ as follows:

$$\nabla \boldsymbol{u}(\boldsymbol{x}, t) = \sum_{k_c} \nabla \boldsymbol{u}^{(k_c)}(\boldsymbol{x}, t). \tag{10}$$

Thus, with Eqs. (9) and (10), the velocity gradient $[\nabla \boldsymbol{u}]_L(t|\boldsymbol{x}_0, t_0)$ along the Lagrangian trajectory is decomposed into the contribution from each scale:

$$[\nabla \boldsymbol{u}]_L(t|\boldsymbol{x}_0, t_0) = \sum_{k_c} [\nabla \boldsymbol{u}^{(k_c)}]_L(t|\boldsymbol{x}_0, t_0), \tag{11}$$

where we introduce $[\nabla \boldsymbol{u}^{(k_c)}]_L(t|\boldsymbol{x}_0, t_0) = \nabla \boldsymbol{u}^{(k_c)}(\boldsymbol{x}_L(t|\boldsymbol{x}_0, t_0), t)$ as the contribution to $[\nabla \boldsymbol{u}]_L(t|\boldsymbol{x}_0, t_0)$ from wave number k_c. According to Eq. (11), we can evaluate the contribution of flows at wave number k_c to the stretching and alignment of dumbbells using $[\nabla \boldsymbol{u}^{(k_c)}]_L(t|\boldsymbol{x}_0, t_0)$. However, it should be noted that the time evolutions of the end-to-end vector $\boldsymbol{R}$ and the center-of-mass $\boldsymbol{R}_G$ of dumbbells [Eqs. (1) and (4)] are based on the raw velocity field $\boldsymbol{u}(\boldsymbol{x}, t)$.

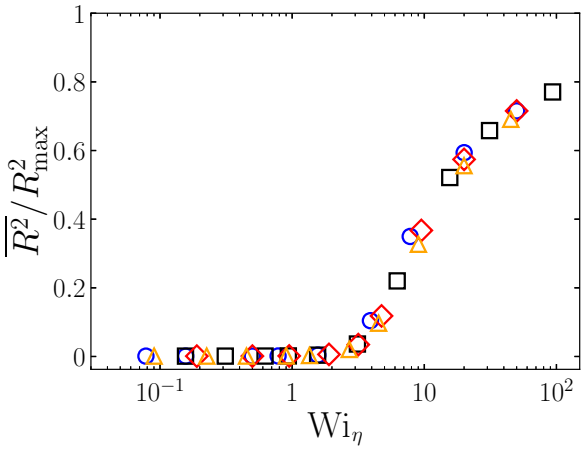

FIG. 2. Mean-squared end-to-end length $\overline{R^2}$ of dumbbells normalized by $R^2_{\max}$ as a function of the Weissenberg number Wi_η for $\mathrm{Re}_\lambda = 30$ (blue circle) and 120 (black square) with forcing $\boldsymbol{f}^{(\mathrm{V})}$ and $\mathrm{Re}_\lambda = 220$ (red diamond) and 310 (orange triangle) with forcing $\boldsymbol{f}^{(\mathrm{I})}$.

A. Polymer stretching

In this subsection, we investigate the scale-dependent contribution of vortices to the stretching of dumbbells. First, we show the average stretching properties of dumbbells in turbulence without using scale-decomposition analysis. Figure 2 shows the mean-squared end-to-end length $\overline{R^2}$ of dumbbells normalized by the square of the maximum extension length $R_{\max}$ as a function of the Weissenberg number $\mathrm{Wi}_\eta = \tau/\tau_\eta$ for different Re_λ. Here, $\overline{(\cdot)}$ denotes the average value over time and all the dumbbells in the system. Figure 2 demonstrates that $\overline{R^2}$ significantly increases with Wi_η for $\mathrm{Wi}_\eta \gtrsim 3$, indicating that the CS transition [38] occurs around $\mathrm{Wi}_\eta = 3$. The observed CS transition around $\mathrm{Wi}_\eta = 3$ is consistent with previous results in homogeneous isotropic turbulence [15]. Interestingly, Wi_η dependence of $\overline{R^2}$ is almost independent of Re_λ and $\boldsymbol{f}$. In other words, the ratio of the relaxation time τ of dumbbells to the Kolmogorov time τ_η (i.e., the characteristic timescale of the smallest-scale vortices in turbulence) determines the degree of the dumbbell stretching. Thus, one may expect that the smallest-scale vortices, which induce the strongest strain-rate fields, dominantly stretch dumbbells. However, as will be described below (see Fig. 3), the stretching mechanism of dumbbells has different characteristics depending on Wi_η. It may be worth noting that Picardo *et al.* [17] reported that dumbbells in turbulent flows and random flows only exhibit a minor difference in the stretching dynamics in spite of the significant non-Gaussianity of turbulence. Their results suggest that for fixed Wi_η, $\overline{R^2}$ does not greatly depend on the detailed characteristics of turbulent flows, which is consistent with the independence of $\overline{R^2}$ from Re_λ and $\boldsymbol{f}$ (Fig. 2).

We have seen that Wi_η determines the average stretching of dumbbells regardless of Re_λ and $\boldsymbol{f}$ (Fig. 2). However, $\overline{R^2}$ does not reveal the scale-dependent effect of vortices on the stretching of dumbbells, which is necessary for understanding the interactions between polymers and each vortex in turbulence. Thus, we investigate the contribution of vortices with different sizes in turbulence to the stretching of dumbbells. With Eq. (1) and the normalized end-to-end vector $\boldsymbol{e}_R = \boldsymbol{R}/R$, we can write the governing equation of R as

$$\frac{dR}{dt} = \gamma R - \frac{1}{2\tau}\frac{R}{1 - R^2/R^2_{\max}} + \sqrt{\frac{4k_BT}{\zeta}}(\boldsymbol{\xi}\cdot\boldsymbol{e}_R) + \frac{4k_BT}{\zeta}\frac{1}{R}, \tag{12}$$

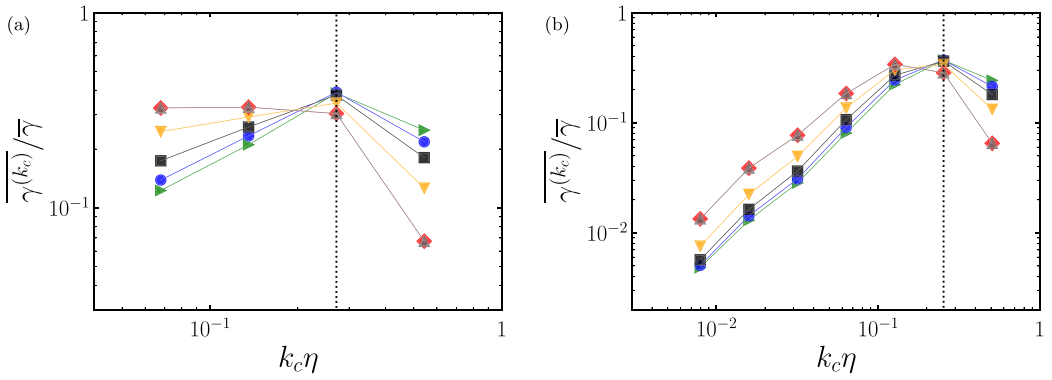

FIG. 3. Contribution $\overline{\gamma^{(k_c)}}$ of flows at wave number k_c to the stretching of dumbbells normalized by the total contribution $\overline{\gamma}$ in turbulent flows with (a) $\mathrm{Re}_\lambda = 30$ and forcing $\boldsymbol{f}^{(\mathrm{V})}$ and (b) $\mathrm{Re}_\lambda = 220$ and forcing $\boldsymbol{f}^{(\mathrm{I})}$ for $\mathrm{Wi}_\eta = 0.1$ (green right triangle), 0.5 (blue circle), 1(black square), 2 (orange inverted triangle), 20 (red diamond), and 50 (gray triangle). The dotted lines in (a) and (b) indicate $k_c\eta = k_c^*\eta$, where k_c^* is defined as the wave number where the average of the largest eigenvalue of the bandpass-filtered strain-rate tensor $\boldsymbol{S}^{(k_c)}$ takes the maximum value: $k_c^* = 4k_f$ and $64\sqrt{2}k_f/5$ in (a) and (b), respectively.

where γ is defined as

$$\gamma = e_{R,j}\left[\frac{\partial u_i}{\partial x_j}\right]_L e_{R,i} = e_{R,j}[S_{ij}]_L e_{R,i}, \tag{13}$$

with $\boldsymbol{S} = \{\boldsymbol{\nabla u} + (\boldsymbol{\nabla u})^{\mathsf{T}}\}/2$ being the strain-rate tensor. From Eq. (12), we can interpret γ as the indicator of the stretching of dumbbells by flows. Using the scale decomposition of the Lagrangian velocity gradient [Eq. (11)], γ is expressed as

$$\gamma = \sum_{k_c} e_{R,j}\left[\frac{\partial u_i^{(k_c)}}{\partial x_j}\right]_L e_{R,i}, \tag{14}$$

where $\boldsymbol{u}^{(k_c)}$ is the bandpass-filtered velocity at wave number k_c. Thus, we define the contribution from flows at wave number k_c as

$$\gamma^{(k_c)} = e_{R,j}\left[\frac{\partial u_i^{(k_c)}}{\partial x_j}\right]_L e_{R,i} = e_{R,j}\left[S_{ij}^{(k_c)}\right]_L e_{R,i}, \tag{15}$$

where $\boldsymbol{S}^{(k_c)} = [\boldsymbol{\nabla u}^{(k_c)} + \{\boldsymbol{\nabla u}^{(k_c)}\}^{\mathsf{T}}]/2$ is the bandpass-filtered strain-rate tensor. In the following, we investigate the scale-dependent contribution to the dumbbell stretching by focusing on $\gamma^{(k_c)}$.

Figure 3(a) shows the average $\overline{\gamma^{(k_c)}}$ of $\gamma^{(k_c)}$ as a function of $k_c\eta$ for $\mathrm{Re}_\lambda = 30$ with forcing $\boldsymbol{f}^{(\mathrm{V})}$, where η is the Kolmogorov length. Here, $\overline{\gamma^{(k_c)}}$ is normalized by $\overline{\gamma}$. The dotted lines in Fig. 3 indicate $k_c\eta = k_c^*\eta$, where k_c^* is defined as the wave number where the average of the largest eigenvalue of the bandpass-filtered strain-rate tensor $\boldsymbol{S}^{(k_c)}$ takes the maximum value [see Fig. 9(b)]. Figure 3(a) demonstrates that for $\mathrm{Wi}_\eta = 0.1$, $\overline{\gamma^{(k_c)}}$ takes the largest value at $k_c \simeq k_c^*(= 0.27\eta^{-1})$. Thus, the smallest-scale vortices have the largest value of $\overline{\gamma^{(k_c)}}$, which appears to be consistent with the observation that τ_η, which corresponds to the characteristic timescale of the smallest-scale vortices, is the essential timescale of turbulence in terms of the average dumbbell stretching (Fig. 2). However, as Wi_η increases, $\overline{\gamma^{(k_c)}}/\overline{\gamma}$ at $k_c \simeq k_c^*$ decreases, and $\overline{\gamma^{(k_c)}}/\overline{\gamma}$ at $k_c \lesssim k_c^*$ increases instead. Finally, $\overline{\gamma^{(k_c)}}/\overline{\gamma}$ at $k_c \lesssim k_c^*$ has comparable and even slightly larger values than that at $k_c \simeq k_c^*$ for $\mathrm{Wi}_\eta = 20$. Therefore, dumbbells with significantly long relaxation times are stretched in a different manner from those with short relaxation times; large-scale vortices also contribute to stretching

dumbbells as well as the smallest-scale vortices. Looking at the results for $\mathrm{Wi}_\eta = 50$, an increase in Wi_η does not affect the behavior of $\overline{\gamma^{(k_c)}}$ for large Wi_η. Since $\overline{\gamma}$ is insensitive to Wi_η for large Wi_η [see Fig. 11(b)], $\overline{\gamma^{(k_c)}}$ is also almost independent of Wi_η for large Wi_η. We will discuss the details of the stretching mechanism of dumbbells, including the saturation of $\overline{\gamma^{(k_c)}}$ for large Wi_η, in Sec. IV A. Figure 3(b) demonstrates that similar characteristics exist in a different system at $\mathrm{Re}_\lambda = 220$ with forcing $\boldsymbol{f}^{(\mathrm{I})}$. For $\mathrm{Wi}_\eta \lesssim 1$, $\overline{\gamma^{(k_c)}}/\overline{\gamma}$ has a similar dependence on k_c regardless of Wi_η and shows the maximum at $k_c \simeq k_c^*(= 0.25\eta^{-1})$, which indicates that the smallest-scale vortices have a dominant effect on the stretching of dumbbells for small Wi_η. In contrast, for $\mathrm{Wi}_\eta \gtrsim 1$, $\overline{\gamma^{(k_c)}}/\overline{\gamma}$ at $k_c \lesssim k_c^*$ increases while $\overline{\gamma^{(k_c)}}/\overline{\gamma}$ at $k_c \simeq k_c^*$ decreases. This indicates that the contributions from large-scale vortices relatively increase for $\mathrm{Wi}_\eta \gtrsim 1$. Although both cases with different Re_λ exhibit the qualitatively same stretching mechanism of dumbbells depending on Wi_η, there is a quantitative difference between Figs. 3(a) and 3(b). The results of $\mathrm{Re}_\lambda = 220$ do not exhibit a significant change in the k_c dependence of $\overline{\gamma^{(k_c)}}/\overline{\gamma}$ compared with those of $\mathrm{Re}_\lambda = 30$. This discrepancy is mainly attributed to the mean flow effect at low Re_λ because in Fig. 3(a), $k_c = 0.068\eta^{-1}$ corresponds to the wave number k_f of the mean flow for forcing $\boldsymbol{f}^{(\mathrm{V})}$. In addition, the observed low-Reynolds-number effect is consistent with the fact that, in general, fully developed turbulence appears for $\mathrm{Re}_\lambda \gtrsim 100$ [39].

In summary, we have demonstrated that the scale-dependent contribution of flows to the stretching of dumbbells varies with the relaxation time τ of dumbbells; for $\tau \lesssim \tau_\eta$, the smallest-scale vortices dominantly stretch dumbbells, whereas for $\tau \gtrsim \tau_\eta$, the contribution from large-scale vortices relatively increases. It should be noted that since we rely on one-way coupled simulations, turbulent flows remain unchanged when changing τ. If we conduct two-way coupled simulations, we will observe a complicatedly combined effect of turbulence modulation by dumbbells and the change in the scale-dependent contribution of flows to the stretching of dumbbells. It is worth emphasizing that we clearly demonstrate the variation of the scale-dependent contribution by changing only τ for a given turbulent flow with various Re_λ and $\boldsymbol{f}$. In Sec. III B, we will focus on the alignment properties of dumbbells to explore the origin of the complex k_c dependence of $\gamma^{(k_c)}$ for different Wi_η (Fig. 3).

B. Polymer alignment

In Sec. III A, the contribution $\overline{\gamma^{(k_c)}}$ of the smallest-scale flows to the stretching of dumbbells predominates for small Wi_η, whereas $\overline{\gamma^{(k_c)}}$ of large-scale flows relatively increases for large Wi_η. In this subsection, we explore the relationship between dumbbells and vortices with different sizes from the alignment perspective to gain further insight into this stretching mechanism. Using the eigenvalue σ_i ($\sigma_1 \geqslant \sigma_2 \geqslant \sigma_3$) of the strain-rate tensor $[\boldsymbol{S}]_L$ and the cosine of the angle $\theta_i \in [0, \pi/2]$ between the end-to-end vector $\boldsymbol{R}$ and the eigenvector $\boldsymbol{e}_i$ of $[\boldsymbol{S}]_L$, we can write γ as

$$\gamma = \sum_{i=1}^{3} \sigma_i (\cos\theta_i)^2. \tag{16}$$

The equality $\sigma_1 + \sigma_2 + \sigma_3 = 0$ holds because of the incompressibility $\boldsymbol{\nabla} \cdot \boldsymbol{u} = 0$ of the fluid. Thus, $\sigma_1 \geqslant 0$ and $\sigma_3 \leqslant 0$, indicating that $\boldsymbol{e}_1$ is the most extensional direction. Since σ_i in Eq. (16) is unaffected by dumbbells in one-way coupled simulations, the change in γ with Wi_η originates from $\cos\theta_i$ (i.e., alignment between $\boldsymbol{R}$ and $[\boldsymbol{S}]_L$). Therefore, we investigate the alignment properties of dumbbells in terms of the hierarchy of coherent vortices using scale-decomposition analysis.

We first demonstrate the alignment between $\boldsymbol{R}$ and $[\boldsymbol{S}]_L$ without the scale decomposition. We show the probability density function (PDF) $P(\cos\theta_i)$ of $\cos\theta_i$ at $\mathrm{Re}_\lambda = 220$ with forcing $\boldsymbol{f}^{(\mathrm{I})}$ in Fig. 4. Figure 4(a) shows that dumbbells preferentially align with $\boldsymbol{e}_1$ for $\mathrm{Wi}_\eta = 0.5$, which means that dumbbells align in the most extensional direction. However, Fig. 4(b) demonstrates that dumbbells preferentially align with $\boldsymbol{e}_2$ rather than $\boldsymbol{e}_1$ for $\mathrm{Wi}_\eta = 20$. This crossover behavior of

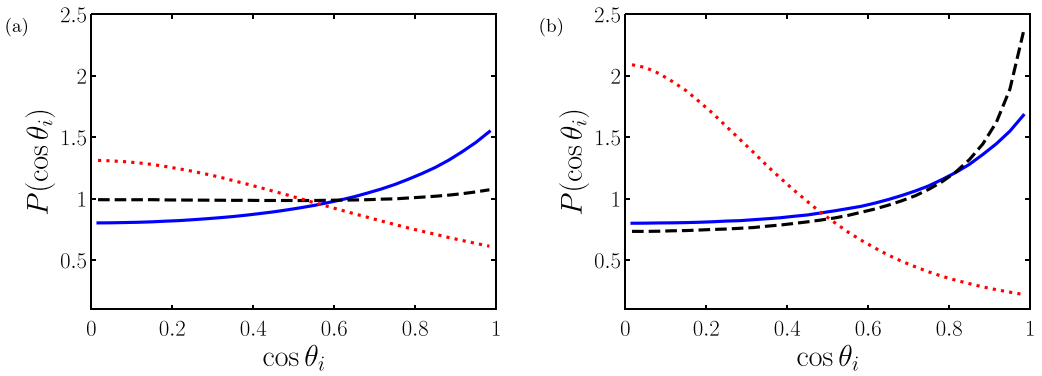

FIG. 4. PDF $P(\cos\theta_i)$ of the cosine of the angle $\theta_i \in [0, \pi/2]$ between the end-to-end vector $\boldsymbol{R}$ and the eigenvectors $\boldsymbol{e}_i$ of the strain-rate tensor for (a) $\mathrm{Wi}_\eta = 0.5$ and (b) 20 at $\mathrm{Re}_\lambda = 220$ with forcing $\boldsymbol{f}^{(\mathrm{I})}$. Different colors correspond to different angles: blue, θ_1; black, θ_2; red, θ_3.

the alignment with an increase in Wi_η has also been observed in two-way coupled simulations [31] as well as in one-way coupled simulations [15]. As observed in previous studies [15,31], $P(\cos\theta_3)$ takes the maximum value at $\cos\theta_3 \simeq 0$ regardless of Wi_η, which indicates that dumbbells tend to be perpendicular to $\boldsymbol{e}_3$. Thus, we focus on the dumbbell alignment with $\boldsymbol{e}_1$ and $\boldsymbol{e}_2$ in terms of the dumbbell stretching [Eq. (16)]. Figure 5 shows the average $\overline{\cos\theta_i}$ of $\cos\theta_i$ as a function of Wi_η for different turbulent flows. We find similar alignment properties irrespective of Re_λ and $\boldsymbol{f}$. Specifically, $\overline{\cos\theta_1} > \overline{\cos\theta_2}$ for $\mathrm{Wi}_\eta \lesssim 3$, whereas $\overline{\cos\theta_1} < \overline{\cos\theta_2}$ for $\mathrm{Wi}_\eta \gtrsim 3$. In addition, $\overline{\cos\theta_1}$ takes the maximum value at $\mathrm{Wi}_\eta \simeq 1$, which is larger than the maximum value of $\overline{\cos\theta_2}$. Valente *et al.* [22] performed DNSs of viscoelastic fluids using the FENE-P model. They demonstrated that for long relaxation times, the eigenvector of the conformation tensor $\boldsymbol{C}$ with the largest eigenvalue tends to align with $\boldsymbol{e}_2$, which is consistent with Fig. 5. They suggested that the weak but persistent strain-rate fields induced by the large-scale flows, rather than the strong but short-lived strain-rate fields induced by the smallest-scale flows, contribute to the stretching of polymers with long relaxation times. However, the quantitative evidence of this scenario has yet to be provided.

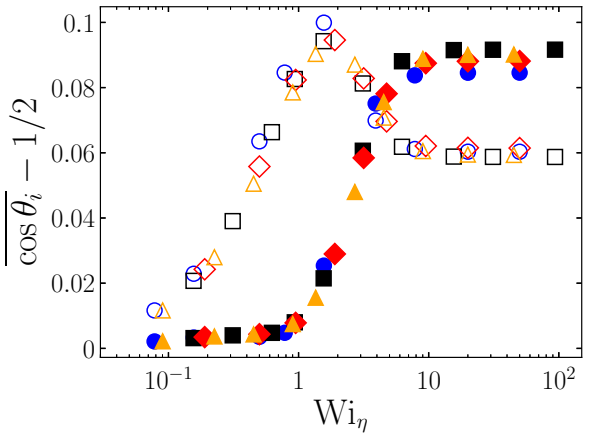

FIG. 5. Average $\overline{\cos\theta_i}$ of $\cos\theta_i$ as a function of the Weissenberg number Wi_η for $\mathrm{Re}_\lambda = 30$ (blue circle) and 120 (black square) with forcing $\boldsymbol{f}^{(\mathrm{V})}$ and $\mathrm{Re}_\lambda = 220$ (red diamond) and 310 (orange triangle) with forcing $\boldsymbol{f}^{(\mathrm{I})}$. The open symbols and the filled symbols correspond to $\overline{\cos\theta_1}$ and $\overline{\cos\theta_2}$, respectively.

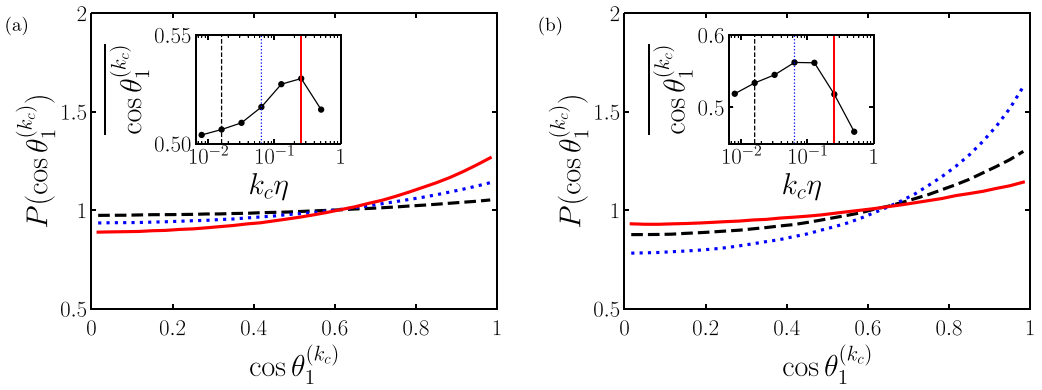

FIG. 6. PDF $P(\cos\theta_1^{(k_c)})$ of the cosine of the angle $\theta_i^{(k_c)} \in [0, \pi/2]$ between the end-to-end vector $\boldsymbol{R}$ and the eigenvector $\boldsymbol{e}_1^{(k_c)}$ of the bandpass-filtered strain-rate tensor at $k_c = k_c^*/16$ (black dashed), $k_c^*/4$ (blue dotted), and k_c^* (red solid) for (a) $\mathrm{Wi}_\eta = 0.5$ and (b) 20 at $\mathrm{Re}_\lambda = 220$ with forcing $\boldsymbol{f}^{(\mathrm{I})}$. Here, $k_c^* = 0.25\eta^{-1}(= 64\sqrt{2}k_f/5)$. The insets show the average $\overline{\cos\theta_1^{(k_c)}}$ of $\cos\theta_1^{(k_c)}$ as a function of $k_c\eta$, and the vertical lines indicate the corresponding wave numbers k_c chosen for $P(\cos\theta_1^{(k_c)})$.

Therefore, we will reveal the origin of the loss of alignment between $\boldsymbol{R}$ and $\boldsymbol{e}_1$ for large Wi_η by using scale-decomposition analysis.

To reveal the alignment properties of dumbbells from the perspective of multiscale features of turbulence, we focus on the eigenvector $\boldsymbol{e}_1^{(k_c)}$ of the bandpass-filtered strain-rate tensor $[\boldsymbol{S}^{(k_c)}]_L$. Figure 6 shows PDF $P(\cos\theta_1^{(k_c)})$ of the cosine of the angle $\theta_1^{(k_c)} \in [0, \pi/2]$ between $\boldsymbol{R}$ and $\boldsymbol{e}_1^{(k_c)}$ at $\mathrm{Re}_\lambda = 220$ with forcing $\boldsymbol{f}^{(\mathrm{I})}$. Here, we show the alignment properties for $k_c = k_c^*$, $k_c^*/4$, and $k_c^*/16$, where $k_c^* = 0.25\eta^{-1}(= 64\sqrt{2}k_f/5)$, corresponding to the smallest scale in turbulence. Figure 6(a) demonstrates that dumbbells align more in the most extensional direction induced by larger k_c for $\mathrm{Wi}_\eta = 0.5$. In other words, smaller-scale vortices have a greater effect on the alignment of dumbbells with small Wi_η. In fact, the inset of Fig. 6(a) demonstrates that $\overline{\cos\theta_1^{(k_c)}}$ monotonically increases up to $k_c \simeq k_c^*$, which is considered as the smallest scale in turbulence. However, Fig. 6(b) shows that for $\mathrm{Wi}_\eta = 20$, dumbbells align most with $\boldsymbol{e}_1^{(k_c)}$ at $k_c = k_c^*/4$, which corresponds to 4 times larger scale than the smallest scale in turbulence. We note that as shown in the inset of Fig. 6(b), $\overline{\cos\theta_1^{(k_c)}}$ at $k_c = k_c^*/2$ has a similar value to that at $k_c = k_c^*/4$, indicating that dumbbells tend to align in the most extensional direction induced by 2–4 times larger vortices than the smallest-scale vortices. Hence, we directly demonstrate that dumbbells with enough relaxation times to be affected by weak large-scale strain-rate fields tend to align in the most extensional direction induced by 2–4 times larger vortices rather than the smallest-scale vortices. In addition, the preferred alignment between $\boldsymbol{R}$ and $\boldsymbol{e}_1^{(k_c)}$ at $k_c = k_c^*/4$ for large Wi_η is consistent with the preferred alignment between $\boldsymbol{R}$ and $\boldsymbol{e}_2$ [Fig. 4(b)] because $\boldsymbol{e}_1^{(k_c)}$ at $k_c = k_c^*/4$ tends to align with $\boldsymbol{e}_2$ [see Fig. 14(b) in Appendix C]. Figure 7 shows the average $\overline{\cos\theta_1^{(k_c)}}$ of $\cos\theta_1^{(k_c)}$ as a function of Wi_η for different Re_λ. We show the results of two wave numbers k_c^*, which corresponds to the smallest scale, and $k_c^*/4$. We find that regardless of Re_λ and $\boldsymbol{f}$, dumbbells preferentially align with $\boldsymbol{e}_1^{(k_c)}$ at $k_c = k_c^*$ for $\mathrm{Wi}_\eta \lesssim 1$, whereas they change the alignment direction to $\boldsymbol{e}_1^{(k_c)}$ at $k_c = k_c^*/4$ for $\mathrm{Wi}_\eta \gtrsim 1$. Note that for the lowest Reynolds number $\mathrm{Re}_\lambda = 30$, dumbbells remarkably align in the most extensional direction induced by large-scale vortices at $k_c = k_c^*/4$ because $k_c^*/4$ is equivalent to the wave number of the mean flow for forcing $\boldsymbol{f}^{(\mathrm{V})}$.

To summarize this subsection, from the perspective of vortices with different sizes in turbulence, the preferential direction of dumbbells depends on Wi_η (Fig. 7), indicating that the alignment of

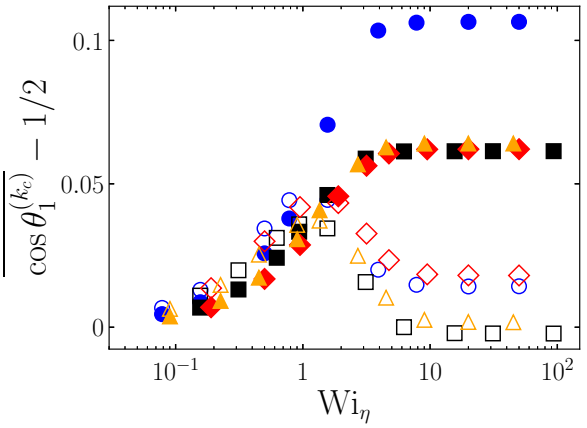

FIG. 7. Average $\overline{\cos\theta_i^{(k_c)}}$ of $\cos\theta_i^{(k_c)}$ as a function of the Weissenberg number Wi_η for $\mathrm{Re}_\lambda = 30$ (blue circle) and 120 (black square) with forcing $\boldsymbol{f}^{(\mathrm{V})}$ and $\mathrm{Re}_\lambda = 220$ (red diamond) and 310 (orange triangle) with forcing $\boldsymbol{f}^{(\mathrm{I})}$. The open symbols indicate the values at $k_c = k_c^*$, where $k_c^* = 4k_f$, $32k_f$, $64\sqrt{2}k_f/5$, and $128\sqrt{2}k_f/5$ for $\mathrm{Re}_\lambda = 30$, 120, 220, and 310, respectively. The filled symbols indicate the values at $k_c^*/4$.

dumbbells is not necessarily determined by the smallest-scale vortices with the largest velocity gradient. Specifically, the alignment of dumbbells is strongly affected by larger-scale vortices for $\mathrm{Wi}_\eta \gtrsim 1$ [Fig. 6(b)], although they preferentially align in the most extensional direction of strain-rate fields induced by the smallest-scale vortices for $\mathrm{Wi}_\eta \lesssim 1$ [Fig. 6(a)]. While we have focused on the instantaneous alignment between dumbbells and the strain-rate tensor, it is also important to consider the cumulative effect of the strain-rate tensor on the dumbbell alignment along the Lagrangian trajectory [40], which is left for a future study. In Sec. IV, we discuss the physical mechanism behind the scale-dependent contribution to the stretching and alignment (Figs. 3 and 7) and the effect of the Reynolds number.

IV. DISCUSSION

A. Persistence of the polymer stretching by vortices with different sizes

In Sec. III B, we have demonstrated that the preferential direction of dumbbells shifts from the most extensional direction induced by the smallest-scale flows to that by 2–4 times larger-scale flows for $\mathrm{Wi}_\eta \gtrsim 1$ (Figs. 6 and 7). Consequently, large-scale flows also contribute to stretching dumbbells for large Wi_η (Fig. 3). Regarding this stretching mechanism, this subsection aims to address the following questions: (i) How do weak large-scale strain-rate fields affect dumbbells? (ii) Why does the contribution of large-scale flows to the stretching of dumbbells saturate when increasing their relaxation time (Fig. 3)? On the first question, Valente *et al.* [22] conjectured that small-scale velocity gradients are not effective in stretching and aligning dumbbells with a long relaxation time in terms of the persistence time of velocity gradients. Thus, we explore the stretching mechanism of dumbbells under the hierarchy of coherent vortices by focusing on the persistent effect of the scale-decomposed strain-rate fields on dumbbells.

First, we quantitatively evaluate the strength and persistence of strain-rate fields induced by different-scale vortices, leaving aside the dynamics of dumbbells. We show the Lagrangian time series of the bandpass-filtered strain-rate tensor $[S_{11}^{(k_c)}]_L$ at $\mathrm{Re}_\lambda = 220$ with forcing $\boldsymbol{f}^{(\mathrm{I})}$ in Fig. 8(a). Here, we choose $k_c = k_c^*$, $k_c^*/2$, and $k_c^*/4$, where $k_c^* = 0.25\eta^{-1} (= 64\sqrt{2}k_f/5)$ corresponding to the smallest scale in turbulence. We also show $[S_{11}]_L$ without the scale decomposition for comparison. Figure 8(a) demonstrates that $[S_{11}^{(k_c)}]_L$ at larger k_c tends to exhibit larger and faster fluctuations, which is consistent with the classical picture of turbulence. In addition, $[S_{11}^{(k_c)}]_L$ at $k_c = k_c^*$, which

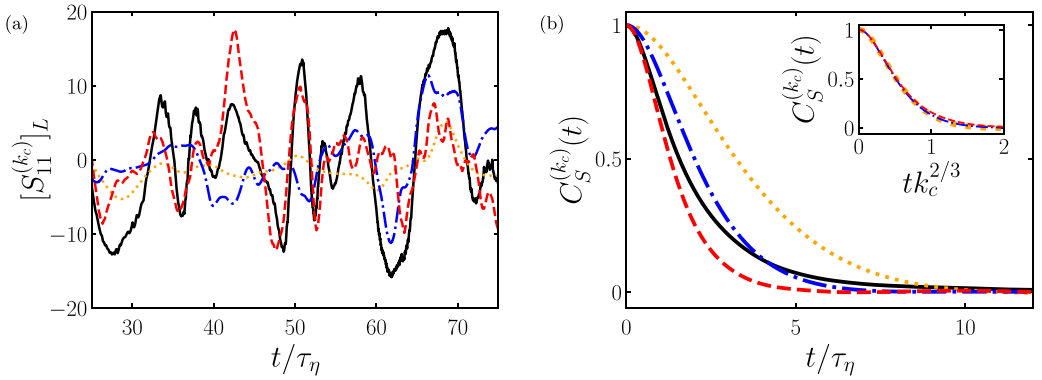

FIG. 8. (a) Bandpass-filtered strain-rate tensor $[S_{11}^{(k_c)}]_L$ as a function of time t normalized by the Kolmogorov time τ_η and (b) autocorrelation function $C_S^{(k_c)}(t)$ of $[\boldsymbol{S}^{(k_c)}]_L$ at $\mathrm{Re}_\lambda = 220$ with forcing $\boldsymbol{f}^{(\mathrm{I})}$ for $k_c = k_c^*/4$ (orange dotted line), $k_c^*/2$ (blue dash-dotted line), and k_c^* (red dashed line), where $k_c^* = 0.25\eta^{-1}$ $(= 64\sqrt{2}k_f/5)$. The black solid line shows the results of the raw strain-rate tensor $[\boldsymbol{S}]_L$. The inset in (b) shows $C_S^{(k_c)}(t)$ as a function of $tk_c^{2/3}$.

corresponds to the length scale of 4η, strongly correlates with S_{11} for $40 \lesssim t/\tau_\eta \lesssim 50$. Interestingly, however, $[S_{11}]_L$ is dominated by $[S_{11}^{(k_c)}]_L$ at $k_c = k_c^*/2$ rather than $k_c = k_c^*$ for $60 \lesssim t/\tau_\eta \lesssim 70$, indicating that the dominant scale in strain-rate fields varies depending on the location and time. It is an interesting future problem to relate the hierarchy of coherent vortices with the detailed characteristics of Lagrangian trajectories, although we concentrate on the average strength and timescale of fluctuations in the following.

To characterize the fluctuations of $[S_{ij}^{(k_c)}]_L$ at different k_c, we calculate the autocorrelation function $C_S^{(k_c)}(t)$ defined as

$$C_S^{(k_c)}(t) = \frac{\overline{[S_{ij}^{(k_c)}]_L(t)[S_{ij}^{(k_c)}]_L(0)}}{\overline{[S_{ij}^{(k_c)}]_L^2}}. \tag{17}$$

Note that $\overline{[S_{ij}^{(k_c)}]_L} = 0$ in the systems considered. Figure 8(b) shows $C_S^{(k_c)}(t)$ for different k_c at $\mathrm{Re}_\lambda = 220$ with forcing $\boldsymbol{f}^{(\mathrm{I})}$. As expected from Fig. 8(a), $C_S^{(k_c)}(t)$ decays faster as k_c increases, which means that strain-rate fields induced by smaller-scale flows fluctuate faster. We also show $C_S(t)$ of $[S_{ij}]_L$ without the scale decomposition in Fig. 8(b) and find that $C_S(t)$ exhibits a slower decay than $C_S^{(k_c)}(t)$ at $k_c = k_c^*$. Since $[S_{ij}]_L$ is the superposition of $[S_{ij}^{(k_c)}]_L$, it is reasonable that $C_S(t)$ is not only affected by the smallest scale but also by larger scales, as suggested from Fig. 8(a).

We then focus on the correlation time $\tau_S^{(k_c)}$ of $[S_{ij}^{(k_c)}]_L$, defined as

$$\tau_S^{(k_c)} = \int_0^\infty C_S^{(k_c)}(t)dt, \tag{18}$$

to systematically compare the fluctuation timescale of $[S_{ij}^{(k_c)}]_L$ at different k_c. Figure 9(a) shows $\tau_S^{(k_c)}/\tau_\eta$ as a function of $k_c\eta$. We find that $\tau_S^{(k_c)}/\tau_\eta$ exhibits a scaling law $\tau_S^{(k_c)}/\tau_\eta \propto (k_c\eta)^{-2/3}$ in the inertial range irrespective of Re_λ and $\boldsymbol{f}$, which is consistent with the Kolmogorov similarity hypothesis. In fact, the inset of Fig. 8(b) demonstrates that $C_S^{(k_c)}(t)$ for various k_c collapses on a single function of $tk_c^{2/3}$. In addition, we also evaluate the strength of the strain-rate fields by the average $\overline{\sigma_1^{(k_c)}}$ of the largest eigenvalue $\sigma_1^{(k_c)}$ of $[\boldsymbol{S}^{(k_c)}]_L$. We show $\tau_\eta\overline{\sigma_1^{(k_c)}}$ as a function of $k_c\eta$ in Fig. 9(b). We confirm a scaling law $\tau_\eta\overline{\sigma_1^{(k_c)}} \propto (k_c\eta)^{2/3}$ derived from the Kolmogorov similarity

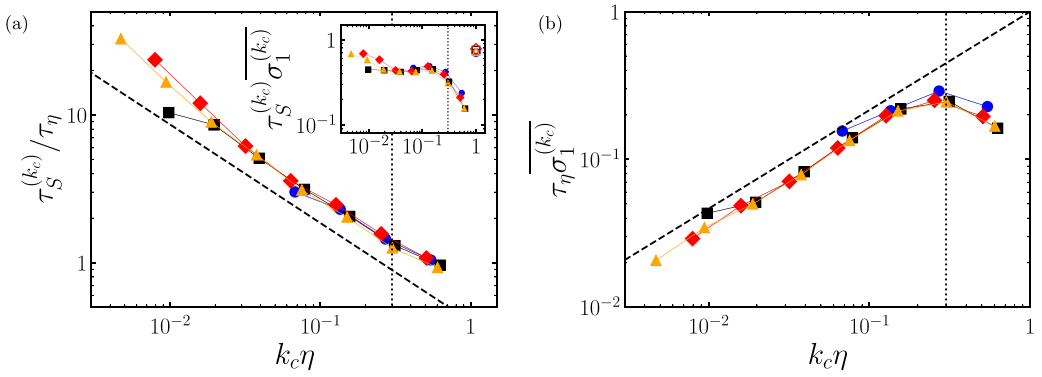

FIG. 9. (a) Correlation time $\tau_S^{(k_c)}$ and (b) average $\overline{\sigma_1^{(k_c)}}$ of the largest eigenvalue $\sigma_1^{(k_c)}$ of the bandpass-filtered strain-rate tensor $[\boldsymbol{S}^{(k_c)}]_L$ nondimensionalized by the Kolmogorov time τ_η as functions of $k_c\eta$ for $\mathrm{Re}_\lambda = 30$ (blue circle) and 120 (black square) with forcing $\boldsymbol{f}^{(\mathrm{V})}$ and $\mathrm{Re}_\lambda = 220$ (red diamond) and 310 (orange triangle) with forcing $\boldsymbol{f}^{(\mathrm{I})}$. The black dashed lines in (a) and (b) indicate $\tau_S^{(k_c)}/\tau_\eta \propto (k_c\eta)^{-2/3}$ and $\tau_\eta\overline{\sigma_1^{(k_c)}} \propto (k_c\eta)^{2/3}$, respectively. The inset in (a) shows the product of $\tau_S^{(k_c)}$ and $\overline{\sigma_1^{(k_c)}}$ as a function of $k_c\eta$. Open symbols indicate the corresponding value $\tau_S\overline{\sigma_1}$ of $[\boldsymbol{S}]_L$. The dotted black lines in (a) and (b) correspond to $k_c\eta = 0.3$.

hypothesis in the inertial range, indicating that smaller-scale vortices induce stronger strain-rate fields. These scaling laws for $\overline{\sigma_1^{(k_c)}}$ and $\tau_S^{(k_c)}$ reveal the trade-off between the strength and the persistence time of the strain-rate fields. The inset of Fig. 9(a) confirms that the product of $\tau_S^{(k_c)}$ and $\overline{\sigma_1^{(k_c)}}$ has an almost constant value ($\simeq 0.4$) in the inertial range $k_f\eta \lesssim k_c\eta \lesssim 0.3$. This indicates that the bandpass-filtered strain-rate tensor at each scale fluctuates with a timescale inversely proportional to the amplitude. We mention in passing that $[\boldsymbol{S}]_L$ also exhibits a similar relationship between the amplitude and timescale of fluctuations, as indicated by the product $\tau_S\overline{\sigma_1}$ of τ_S and $\overline{\sigma_1}$ for the raw strain-rate tensor $[\boldsymbol{S}]_L$ shown in the inset of Fig. 9(a). In summary, we provide evidence that larger-scale strain-rate fields are weaker [Fig. 9(b)] but more persistent [Fig. 9(a)], which gives a clue to the reason why larger-scale flows become influential in the dynamics of dumbbells as Wi_η increases.

However, it is worth emphasizing that $\tau_S^{(k_c)}$ is the characteristic timescale of strain-rate fields itself. To quantitatively answer the two questions mentioned at the beginning of this subsection, we directly quantify how persistently different-scale flows stretch dumbbells. Since $\gamma^{(k_c)}$ represents the contribution of flows at wave number k_c to the stretching of dumbbells, we evaluate the persistence of $\gamma^{(k_c)}$ for various Wi_η. For this purpose, we define the autocorrelation function $C_\gamma^{(k_c)}(t)$ of $\gamma^{(k_c)}$ as

$$C_\gamma^{(k_c)}(t) = \frac{\overline{\{\gamma^{(k_c)}(t) - \overline{\gamma^{(kc)}}\}\{\gamma^{(k_c)}(0) - \overline{\gamma^{(kc)}}\}}}{\overline{\{\gamma^{(k_c)}\}^2}}. \tag{19}$$

Figure 10(a) shows $C_\gamma^{(k_c)}(t)$ for $\mathrm{Wi}_\eta = 10$. To characterize the persistence of $\gamma^{(k_c)}$, we introduce the correlation time $\tau_\gamma^{(k_c)}$ of $\gamma^{(k_c)}$ defined as

$$\tau_\gamma^{(k_c)} = \int_0^\infty C_\gamma^{(k_c)}(t)dt. \tag{20}$$

Larger $\tau_\gamma^{(k_c)}$ means that flows at wave number k_c persistently stretch dumbbells more. Figure 10(b) shows $\tau_\gamma^{(k_c)}/\tau_\eta$ as a function of $k_c\eta$ for various Wi_η. We find that $\tau_\gamma^{(k_c)}/\tau_\eta$ exhibits a different behavior depending on Wi_η. We now consider k_c dependence of $\tau_\gamma^{(k_c)}/\tau_\eta$ for $\mathrm{Wi}_\eta \lesssim 1$ and $\mathrm{Wi}_\eta \gtrsim 1$ by focusing on the competition between the fluctuation timescales of dumbbells and the bandpass-filtered

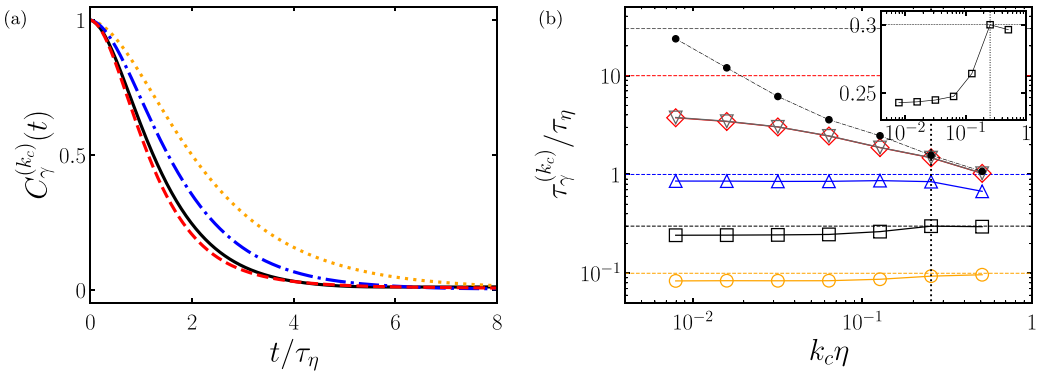

FIG. 10. (a) Autocorrelation function $C_\gamma^{(k_c)}(t)$ of $\gamma^{(k_c)}$ for $\mathrm{Wi}_\eta = 10$. Different lines denote different values of the wave number: orange dotted line, $k_c = k_c^*/4$; blue dash-dotted line, $k_c^*/2$; red dashed line, k_c^*. Here, $k_c^* = 0.25\eta^{-1}(= 64\sqrt{2}k_f/5)$. The black solid line shows the autocorrelation function $C_\gamma(t)$ of γ. (b) Correlation time $\tau_\gamma^{(k_c)}$ of $\gamma^{(k_c)}$ normalized by the Kolmogorov time τ_η as a function of $k_c\eta$ for $\mathrm{Wi}_\eta = 0.1$ (orange circle), 0.3 (black square), 1 (blue triangle), 10 (red diamond), and 30 (gray inverted triangle). For clarity, $\tau_\gamma^{(k_c)}/\tau_\eta$ for $\mathrm{Wi}_\eta = 0.3$ is replotted in the inset in a linear scale. The horizontal dashed lines indicate τ/τ_η for each case. The vertical black dotted lines indicate $k_c\eta = k_c^*\eta$. The black filled circles indicate $\tau_S^{(k_c)}/\tau_\eta$ for comparison. The results are for turbulence at $\mathrm{Re}_\lambda = 220$ with forcing $\boldsymbol{f}^{(\mathrm{I})}$.

strain-rate tensor. For $\mathrm{Wi}_\eta \lesssim 1$, $\tau_\gamma^{(k_c)}$ is of the same order as the relaxation time τ of dumbbells regardless of k_c, as demonstrated by the dotted lines in Fig. 10(b). Since τ of dumbbells with $\mathrm{Wi}_\eta \lesssim 1$ is shorter than $\tau_S^{(k_c)}$ for any k_c [Fig. 9(a)], flows at different scales can only persistently stretch dumbbells over a period of $O(\tau)$ regardless of their scales due to the faster relaxation of dumbbells than the fluctuations of flows. Thus, the persistence of large-scale vortices is not relevant, and only the strength of the strain-rate fields is a crucial factor for stretching dumbbells. This is why the smallest-scale vortices with the largest velocity gradient mainly affect the dynamics of dumbbells for $\mathrm{Wi}_\eta \lesssim 1$ (Fig. 3). Incidentally, a close look shows that $\tau_\gamma^{(k_c)}/\tau_\eta$ for $\mathrm{Wi}_\eta = 0.3$ takes the maximum value at $k_c \simeq k_c^*$, which corresponds to the smallest scale in turbulence [see also the inset of Fig. 10(b)]. In contrast, for $\mathrm{Wi}_\eta \gtrsim 1$, $\tau_\gamma^{(k_c)}$ increases as k_c decreases. The results demonstrate that since there exists k_c such that $\tau \gtrsim \tau_S^{(k_c)}$ for $\mathrm{Wi}_\eta \gtrsim 1$, large-scale flows at the wave number k_c can stretch and align dumbbells more persistently than the smallest-scale flows at k_c^* because $\tau_S^{(k_c)} \gtrsim \tau_S^{(k_c^*)}$. This increase in $\tau_\gamma^{(k_c)}$ at small k_c explains the reason why the contribution from large-scale flows to the stretching of dumbbells relatively increases for $\mathrm{Wi}_\eta \gtrsim 1$ (Fig. 3). However, $\tau_\gamma^{(k_c)}$ exhibits a weaker growth than the correlation time $\tau_S^{(k_c)}$ of the bandpass-filtered strain-rate tensor $[\boldsymbol{S}^{(k_c)}]_L$, as shown in Fig. 10(b). We attribute this weak growth of $\tau_\gamma^{(k_c)}$ to the fluctuation of $\boldsymbol{e}_R$ with the timescale of τ_η. In the governing equation of $\boldsymbol{R}$ [Eq. (1)], since $\kappa_{ij} = O(1/\tau_\eta)$, $\boldsymbol{\kappa}\cdot\boldsymbol{R}$ becomes dominant over $\boldsymbol{R}/\{2\tau(1 - R^2/R_{\max}^2)\}$ when $\mathrm{Wi}_\eta = \tau/\tau_\eta \gg 1$. Thus, for $\mathrm{Wi}_\eta \gg 1$, $\boldsymbol{R}(t)$ fluctuates with the timescale of the temporal fluctuations of $\boldsymbol{\kappa}(t)$, i.e., τ_η. Consequently, the correlation time $\tau_\gamma^{(k_c)}$ of $\gamma^{(k_c)} = \boldsymbol{e}_R \cdot [\nabla \boldsymbol{u}^{(k_c)}]_L \cdot \boldsymbol{e}_R$ at $k_c \ll k_c^*$ cannot be as long as the correlation time $\tau_S^{(k_c)}$ of $[\boldsymbol{S}^{(k_c)}]_L$ for $\mathrm{Wi}_\eta \gg 1$. In other words, while large-scale vortices attempt to stretch dumbbells persistently, neighboring smallest-scale vortices quickly rotate dumbbells, thus leading to the decorrelation between the direction of dumbbells and the most extensional direction of the strain-rate fields at large scales. Thus, in spite of their persistence, larger-scale vortices than the smallest-scale vortices cannot be effective in stretching dumbbells even when Wi_η is significantly large, although their relative contribution increases for $\mathrm{Wi}_\eta \gtrsim 1$. To summarize this subsection, the correlation time $\tau_\gamma^{(k_c)}$ of $\gamma^{(k_c)}$ explains the relaxation-time dependence of the stretching mechanism of dumbbells by vortices with different sizes.

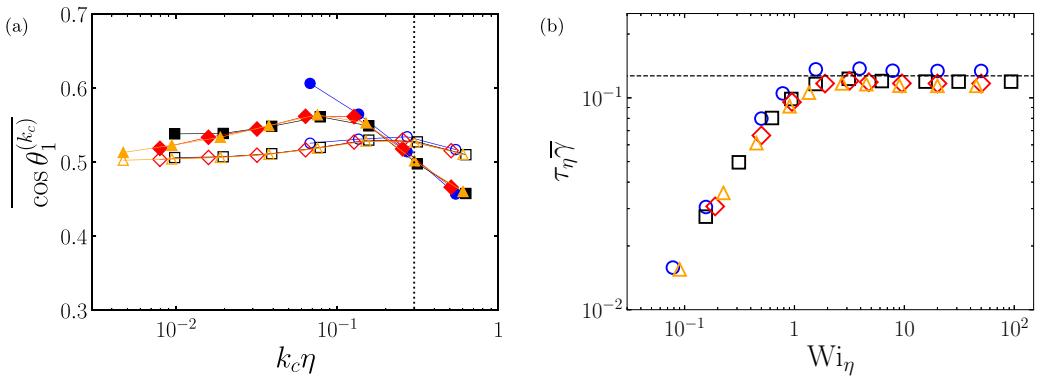

FIG. 11. (a) Average $\overline{\cos\theta_1^{(k_c)}}$ of $\cos\theta_1^{(k_c)}$ as a function of $k_c\eta$ and (b) average $\overline{\gamma}$ of γ nondimensionalized by τ_η as a function of the Weissenberg number Wi_η for $\mathrm{Re}_\lambda = 30$ (blue circle) and 120 (black square) with forcing $\boldsymbol{f}^{(\mathrm{V})}$ and $\mathrm{Re}_\lambda = 220$ (red diamond) and 310 (orange triangle) with forcing $\boldsymbol{f}^{(\mathrm{I})}$. The black dotted line in (a) corresponds to $k_c\eta = 0.3$. In (a), the open and filled symbols correspond to $\mathrm{Wi}_\eta = 0.5$ and 20, respectively. The black dashed line in (b) indicates $\tau_\eta\overline{\gamma} = 0.127$, which corresponds to the value for passive vector elements in isotropic turbulence [41].

B. Reynolds-number dependence

In Sec. III B, the evaluation of the alignment between dumbbells and the bandpass-filtered strain-rate tensor has revealed that the scale of flows relevant to the alignment of dumbbells depends on their relaxation time (Figs. 6 and 7). The results indicate that dumbbells undergo the hierarchy of coherent vortices in turbulence. Meanwhile, the mean-squared end-to-end length $\overline{R^2}$ of dumbbells as a function of Wi_η collapses on a single curve irrespective of Re_λ and $\boldsymbol{f}$ (Fig. 2). In this subsection, we discuss the effect of Re_λ on the stretching and alignment of dumbbells in terms of the hierarchy of coherent vortices.

Using the scale decomposition [Eq. (15)] and the eigenvalues of the strain-rate tensor [Eq. (16)], we can write the contribution γ of flows to the stretching of dumbbells as

$$\gamma = \sum_{k_c} \gamma^{(k_c)} = \sum_{k_c} \sum_{i=1}^{3} \sigma_i^{(k_c)} \left\{\cos\theta_i^{(k_c)}\right\}^2. \tag{21}$$

With $\widetilde{t} = t/\tau_\eta$, $\widetilde{R} = R/R_0$, and $\widetilde{R}_{\max} = R_{\max}/R_0$, we render Eq. (12) dimensionless as

$$\frac{d\widetilde{R}}{d\widetilde{t}} = \left\{ \sum_{k_c} \sum_{i=1}^{3} \tau_\eta \sigma_i^{(k_c)} \left(\cos\theta_i^{(k_c)}\right)^2 \right\} \widetilde{R} - \frac{1}{2\mathrm{Wi}_\eta} \frac{\widetilde{R}}{1 - \widetilde{R}^2/\widetilde{R}_{\max}^2} + \frac{1}{\mathrm{Wi}_\eta} \frac{1}{\widetilde{R}}. \tag{22}$$

Here, $R_0 = \sqrt{k_B T/H}$, and we ignore the stochastic term for simplicity. We have confirmed that $\tau_\eta\sigma_1^{(k_c)}$, which is the dominant contribution to the stretching in Eq. (22), exhibits a common scaling law $\tau_\eta\overline{\sigma_1^{(k_c)}} = C(k_c\eta)^{2/3}$ in the inertial range irrespective of Re_λ, where C is a universal dimensionless constant [Fig. 9(b)]. Therefore, for fixed Wi_η, only $\cos\theta_i^{(k_c)}$ can be a cause of Re_λ dependence in Eq. (22). We show $\overline{\cos\theta_1^{(k_c)}}$ as a function of $k_c\eta$ for $\mathrm{Wi}_\eta = 0.5$ and 20 in Fig. 11(a). As already shown in Figs. 6 and 7, dumbbells tend to align in the most extensional direction induced by 2–4 times larger vortices rather than the smallest-scale vortices in turbulence (i.e., $k_c\eta \simeq 0.3$) for $\mathrm{Wi}_\eta = 20$. Note that the mean flow is still dominant due to the low-Reynolds-number effect for $\mathrm{Re}_\lambda = 30$, thus leading to a remarkable alignment in the most extensional direction at the forcing scale k_f. Consequently, as expected from Eq. (21), the scale-dependent contribution $\overline{\gamma^{(k_c)}}/\overline{\gamma}$ to the

stretching of dumbbells for $\mathrm{Re}_\lambda = 30$ exhibits drastic changes [Fig. 3(a)] compared with higher Re_λ [Fig. 3(b)]. To summarize, $\overline{\gamma^{(k_c)}}$ has Re_λ dependence through the alignment of dumbbells, especially for low Re_λ. In contrast, Fig. 11(b) shows that $\tau_\eta\overline{\gamma}$, which corresponds to the sum of each contribution $\overline{\gamma^{(k_c)}}$, is almost independent of Re_λ for fixed Wi_η, although $\tau_\eta\overline{\gamma}$ has a slightly larger value for $\mathrm{Re}_\lambda = 30$ than that for higher Re_λ. This collapse of $\tau_\eta\overline{\gamma}$ for different Re_λ means that Eq. (22) does not possess a significant Re_λ dependence and is almost dominated by Wi_η. This is why the mean-squared end-to-end length $\overline{R^2}$ follows a single function regardless of Re_λ. In other words, although Re_λ can change the scale-dependent contribution $\overline{\gamma^{(k_c)}}$ to the stretching of dumbbells for fixed Wi_η, the resultant change is not so large to alter the overall contribution $\overline{\gamma}$, thus leading to the independence of Re_λ. However, it is worth emphasizing again that although Wi_η dominates the average stretching of dumbbells, the contribution to the stretching of dumbbells from vortices with different sizes in turbulence exhibits a nontrivial scale dependence (Fig. 3). The scale-dependent contribution to the dynamics of polymers will be crucial for understanding turbulence modulation in terms of the interactions between vortices and polymers. Before closing this subsection, it is worth mentioning that for $\mathrm{Wi}_\eta \gtrsim 3$, $\tau_\eta\overline{\gamma}$ takes the value similar to that found for passive vector elements in isotropic turbulence [41], as indicated by the black dashed line in Fig. 11(b). This tendency is consistent with the fact that the governing equation of $\boldsymbol{R}$ for dumbbells [Eq. (1)] asymptotically approaches that for passive vector elements in the limit of large τ (i.e., $d\boldsymbol{R}/dt = \boldsymbol{\kappa}\cdot\boldsymbol{R}$).

V. CONCLUSIONS

We have investigated the stretching and alignment of FENE dumbbell models in turbulence using the Brownian dynamics simulations. An essential ingredient for this study is scale-decomposition analysis, which reveals the behavior of dumbbells in terms of the hierarchy of coherent vortices in turbulence. We have found that the mean-squared end-to-end length $\overline{R^2}$ is determined by the Weissenberg number $\mathrm{Wi}_\eta = \tau/\tau_\eta$, defined as the ratio of the relaxation time τ of dumbbells to the Kolmogorov time τ_η, regardless of the Reynolds number Re_λ based on the Taylor microscale and the type of external force $\boldsymbol{f}$ (Fig. 2). One might expect that this universality indicates that the smallest-scale vortices dominate the stretching of dumbbells. However, we have demonstrated that larger-scale vortices also affect the dynamics of dumbbells when τ exceeds τ_η. For $\mathrm{Wi}_\eta \lesssim 1$, the contribution $\overline{\gamma^{(k_c)}}$ [Eq. (15)] of flows at wave number k_c to the stretching of dumbbells takes the maximum value at a wave number k_c^* which corresponds to the smallest scale in turbulence. In contrast, $\overline{\gamma^{(k_c)}}$ at smaller k_c, which corresponds to larger length scales, relatively increases for $\mathrm{Wi}_\eta \gtrsim 1$ (Fig. 3). To explore the origin of this nontrivial scale dependence, we have evaluated the alignment between dumbbells and the bandpass-filtered strain-rate tensor $[\boldsymbol{S}^{(k_c)}]_L$ for various Re_λ and Wi_η (Figs. 6 and 7). For $\mathrm{Wi}_\eta \lesssim 1$, dumbbells preferentially align in the most extensional direction induced by the smallest-scale vortices. In contrast, for $\mathrm{Wi}_\eta \gtrsim 1$, dumbbells tend to align in the most extensional direction induced by 2–4 times larger vortices than the smallest-scale vortices. This shift of a preferential direction of dumbbells is consistent with the previously reported results [15,22,31] that in turbulent flows, dumbbells with a long relaxation time exhibit a preferential alignment with the the eigenvector $\boldsymbol{e}_2$ of the raw strain-rate tensor $[\boldsymbol{S}]_L$ with the second largest eigenvalue (Figs. 4 and 5), because $\boldsymbol{e}_2$ tends to align with the eigenvector $\boldsymbol{e}_1^{(k_c)}$ of $[\boldsymbol{S}^{(k_c)}]_L$ at $k_c = k_c^*/4$ with the largest eigenvalue [Fig. 14(b) in Appendix C].

We have explained the scale-dependent effect of flows on dumbbells depending on their relaxation time by focusing on how persistently each-scale flow stretches dumbbells. To characterize the strain-rate fields at different scales, we have analyzed the temporal fluctuations of $[\boldsymbol{S}^{(k_c)}]_L$ along the Lagrangian trajectories (Fig. 8). As expected from the Kolmogorov similarity hypothesis, smaller-scale vortices induce stronger strain-rate fields [Fig. 9(b)] with shorter correlation times $\tau_S^{(k_c)}$ [Fig. 9(a)]. In terms of these scale-dependent characteristics of flows, we have investigated the persistence of the stretching process of dumbbells by the strain-rate fields at different scales.

The most important conclusion is that the correlation time $\tau_\gamma^{(k_c)}$ of $\gamma^{(k_c)} = \boldsymbol{e}_R \cdot [\nabla \boldsymbol{u}^{(k_c)}]_L \cdot \boldsymbol{e}_R$ reveals the stretching mechanism of dumbbells by vortices with different sizes [Fig. 10(b)]. For $\mathrm{Wi}_\eta \lesssim 1$, $\tau_\gamma^{(k_c)} = O(\tau)$ irrespective of k_c because $\boldsymbol{e}_R$ fluctuates with the timescale of τ faster than $[\nabla \boldsymbol{u}^{(k_c)}]_L$, i.e., $\tau \lesssim \tau_S^{(k_c)}$ for any k_c. Thus, the smallest-scale flows most contribute to the stretching of dumbbells (Fig. 3) because only the strength of the strain-rate fields is relevant to the contribution to the stretching of dumbbells. In contrast, for $\mathrm{Wi}_\eta \gtrsim 1$, $\tau_\gamma^{(k_c)}$ increases as k_c decreases because of the persistence of large-scale flows. Consequently, the contribution of large-scale flows to the stretching of dumbbells relatively increases for $\mathrm{Wi}_\eta \gtrsim 1$ (Fig. 3). However, $\tau_\gamma^{(k_c)}$ at $k_c \ll k_c^*$ is much shorter than $\tau_S^{(k_c)}$. This indicates that larger-scale vortices than the smallest-scale vortices cannot fully utilize their persistence because $\boldsymbol{e}_R$ fluctuates with the timescale of τ_η due to neighboring smallest-scale vortices and loses the correlation with the larger-scale strain-rate fields. Thus, the contribution from large-scale vortices gets saturated when increasing Wi_η (Fig. 3). In addition, we have demonstrated that this scale-dependent effect of vortices on dumbbells is almost independent of Re_λ and $\boldsymbol{f}$, although there exists a slight effect of the mean flow only for low Re_λ (Fig. 11).

One-way coupled simulations have allowed us to systematically investigate the scale-dependent contribution of vortices to the stretching and alignment of dumbbells. There will be other scenarios on the interactions between polymers and vortices in realistic two-way coupled cases. When polymer solutions are dilute enough to have little effect on turbulence, polymers with a relaxation time longer than the Kolmogorov time will interact with not only the smallest-scale vortices but also larger-scale vortices, as demonstrated in this study. However, when their concentration is large enough to suppress turbulence, the smallest-scale vortices will almost disappear due to the interactions. As a result, polymers will mainly interact with larger-scale vortices simply because the original smallest-scale vortices do not exist, which is a qualitatively distinct mechanism from that demonstrated in this paper. We should also note a qualitative change in turbulent carrier flows due to polymers. The present paper assumes the Kolmogorov scaling $E(k) \propto k^{-5/3}$ in the inertial range, where $E(k)$ is the energy spectrum at wave number k. Thus, smaller-scale vortices induce stronger strain-rate fields, as confirmed in Fig. 9(b). However, since some polymer solutions are known to exhibit a steeper scaling law [42,43], there will be a case where the scale-dependence of the velocity gradient is reversed, which will bring about a significantly different picture of the interactions between polymers and vortices. In general, these qualitatively distinct effects coexist depending on the parameters of polymers and flows. Therefore, it is a crucial future study to apply the scale-decomposition analysis proposed in this paper to various systems.

ACKNOWLEDGMENTS

The present paper was supported in part by Japan Society for the Promotion of Science Grants-in-Aid for Scientific Research (Grants No. 20H02068 and No. 21J21061). The simulations were conducted under the auspices of the National Institute for Fusion Science Collaboration Research Programs (NIFS22KISS010).

APPENDIX A: EFFECT OF THE MAXIMUM EXTENSION LENGTH OF DUMBBELLS

In the main text, we have shown the stretching and alignment of dumbbells for $R_{\max}^2/R_0^2 = 3000$. Here, we demonstrate that the choice of $R_{\max}$ has little effect on our conclusion. Figure 12 shows $\overline{\gamma^{(k_c)}}/\overline{\gamma}$ and $\overline{\cos\theta_1^{(k_c)}}$ as functions of $k_c\eta$ for various $R_{\max}$ at $\mathrm{Re}_\lambda = 220$ with forcing $\boldsymbol{f}^{(1)}$. We confirm that the scale-dependent contribution to the stretching and alignment of dumbbells is almost independent of $R_{\max}$. However, we should note that our results are based on one-way coupled simulations. For two-way coupled simulations, since the stress tensor from dumbbells depends on $R_{\max}$, the resultant carrier velocity field varies with $R_{\max}$, thus leading to $R_{\max}$ dependence of the stretching and alignment of dumbbells.

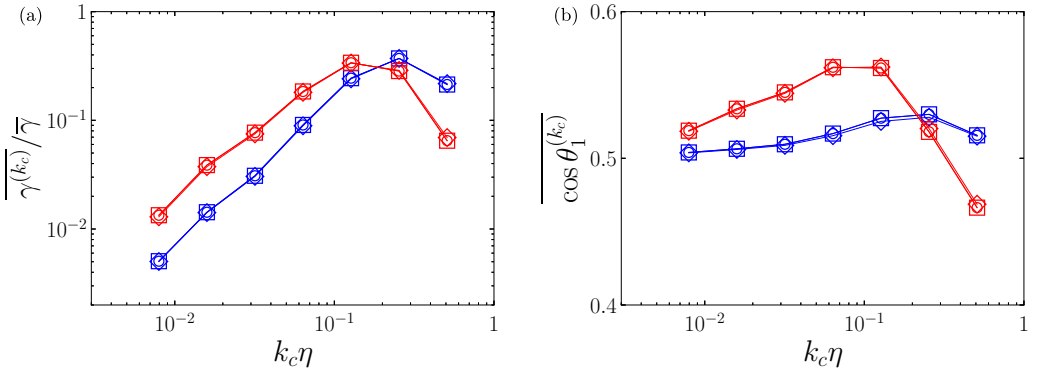

FIG. 12. (a) Scale-dependent contribution $\overline{\gamma^{(k_c)}}$ to the stretching of dumbbells normalized by the total contribution $\overline{\gamma}$ and (b) average $\overline{\cos\theta_1^{(k_c)}}$ of $\cos\theta_1^{(k_c)}$ as functions of $k_c\eta$ at $\mathrm{Re}_\lambda = 220$ with forcing $\boldsymbol{f}^{(\mathrm{I})}$ for $R^2_{\max}/R^2_0 = 50$ (diamond), 3000 (circle), and 100000 (square). Blue and red symbols correspond to $\mathrm{Wi}_\eta = 0.5$ and 20, respectively.

APPENDIX B: EFFECT OF THE BANDWIDTH

In the main text, we have shown the scale-dependent contribution of flows to the stretching and alignment of dumbbells using the passband $[k_c/\sqrt{2}, \sqrt{2}k_c]$ with the logarithmic bandwidth $\Delta(\log_{10} k_c) = \log_{10} 2$. Here, we confirm that our conclusions are insensitive to the choice of the bandwidth. Figure 13 shows $\overline{\gamma^{(k_c)}}/\{\overline{\gamma}\Delta(\log_{10} k_c)\}$ and $\overline{\cos\theta_1^{(k_c)}}$ as functions of $k_c\eta$ for $\Delta(\log_{10} k_c) = \log_{10} 2$ and $\log_{10}\sqrt{2}$ at $\mathrm{Re}_\lambda = 220$ with forcing $\boldsymbol{f}^{(\mathrm{I})}$. To compensate for the difference in $\Delta(\log_{10} k_c)$, $\overline{\gamma^{(k_c)}}/\overline{\gamma}$ is divided by $\Delta(\log_{10} k_c)$ in Fig. 13(a). We confirm that $\overline{\gamma^{(k_c)}}/\{\overline{\gamma}\Delta(\log_{10} k_c)\}$ for different $\Delta(\log_{10} k_c)$ exhibits excellent agreement. In addition, $\overline{\cos\theta_1^{(k_c)}}$ also shows a qualitatively similar tendency regardless of $\Delta(\log_{10} k_c)$, although quantitative values of $\overline{\cos\theta_1^{(k_c)}}$ slightly depend on $\Delta(\log_{10} k_c)$ due to the nonlinear decomposition of $\cos\theta_1^{(k_c)}$ unlike $\gamma^{(k_c)}$. Therefore, our conclusions about the increased contribution from large-scale flows for $\mathrm{Wi}_\eta \gtrsim 1$ are independent of the choice of the passband.

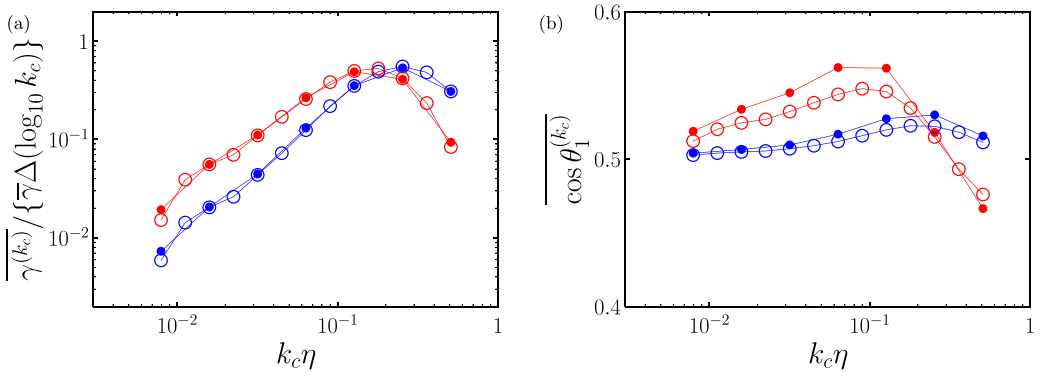

FIG. 13. (a) Scale-dependent contribution $\overline{\gamma^{(k_c)}}$ to the stretching of dumbbells normalized by the total contribution $\overline{\gamma}$ and the logarithmic bandwidth $\Delta(\log_{10} k_c)$ and (b) average $\overline{\cos\theta_1^{(k_c)}}$ of $\cos\theta_1^{(k_c)}$ as functions of $k_c\eta$ at $\mathrm{Re}_\lambda = 220$ with forcing $\boldsymbol{f}^{(\mathrm{I})}$ for $\Delta(\log_{10} k_c) = \log_{10} 2$ (filled) and $\log_{10}\sqrt{2}$ (open). Blue and red symbols correspond to $\mathrm{Wi}_\eta = 0.5$ and 20, respectively.

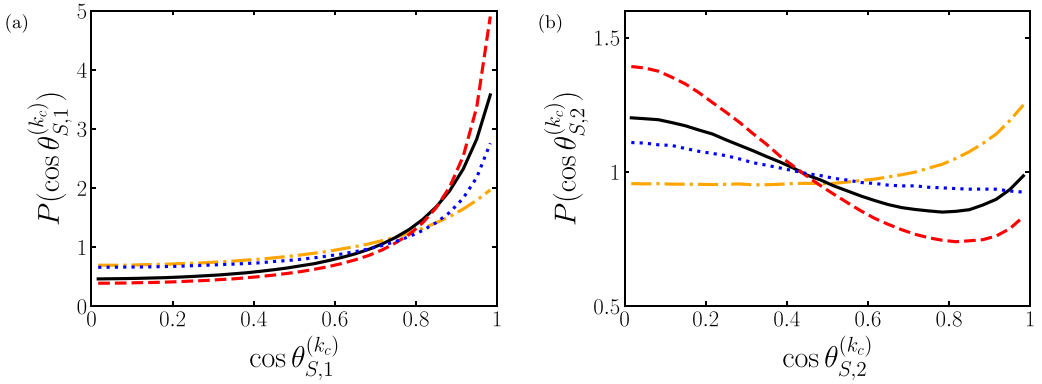

FIG. 14. (a) PDF $P(\cos\theta_{S,1}^{(k_c)})$ of the cosine of the angle $\theta_{S,1}^{(k_c)} \in [0, \pi/2]$ between the eigenvector $\boldsymbol{e}_1$ of the strain-rate tensor and the eigenvector $\boldsymbol{e}_1^{(k_c)}$ of the bandpass-filtered strain-rate tensor and (b) PDF $P(\cos\theta_{S,2}^{(k_c)})$ of the cosine of the angle $\theta_{S,2}^{(k_c)} \in [0, \pi/2]$ between $\boldsymbol{e}_2$ and $\boldsymbol{e}_1^{(k_c)}$ at $\mathrm{Re}_\lambda = 220$ with forcing $\boldsymbol{f}^{(\mathrm{I})}$ for $k_c = k_c^*/4$ (orange dash-dotted), $k_c^*/2$ (black solid), k_c^* (red dashed), and $2k_c^*$ (blue dotted), where $k_c^* = 0.25k_\eta (= 64\sqrt{2}k_f/5)$.

APPENDIX C: ALIGNMENT PROPERTIES OF THE BANDPASS-FILTERED STRAIN-RATE TENSOR

In this Appendix, we describe the alignment properties of the bandpass-filtered strain-rate tensor $\boldsymbol{S}^{(k_c)}$. Figure 14(a) shows the PDF $P(\cos\theta_{S,1}^{(k_c)})$ of the cosine of the angle $\theta_{S,1}^{(k_c)} \in [0, \pi/2]$ between $\boldsymbol{e}_1$ and $\boldsymbol{e}_1^{(k_c)}$ for $k_c = k_c^*/4$, $k_c^*/2$, k_c^*, and $2k_c^*$, where $k_c^* = 0.25\eta^{-1} (= 64\sqrt{2}k_f/5)$. For k_c shown in Fig. 14(a), $P(\cos\theta_{S,1}^{(k_c)})$ has the maximum value at $\cos\theta_{S,1}^{(k_c)} \simeq 1$. The alignment tendency between $\boldsymbol{e}_1$ and $\boldsymbol{e}_1^{(k_c)}$ is reasonable because $\boldsymbol{S}$ is a superposition of $\boldsymbol{S}^{(k_c)}$. Notably, for $k_c \leqslant k_c^*$, $P(\cos\theta_{S,1}^{(k_c)})$ at $\cos\theta_{S,1}^{(k_c)} \simeq 1$ increases with k_c, which is consistent with the fact that smaller-scale flows (i.e., flows at larger k_c) induce stronger strain-rate fields [Fig. 9(b)]. In contrast, increasing k_c further to $2k_c^*$ reduces $P(\cos\theta_{S,1}^{(k_c)})$ at $\cos\theta_{S,1}^{(k_c)} \simeq 1$ because $2k_c^*$ is almost located in the dissipation range. We also show the PDF $P(\cos\theta_{S,2}^{(k_c)})$ of the cosine of the angle $\theta_{S,2}^{(k_c)} \in [0, \pi/2]$ between $\boldsymbol{e}_2$ and $\boldsymbol{e}_1^{(k_c)}$ in Fig. 14(b). Unlike $P(\cos\theta_{S,1}^{(k_c)})$, $P(\cos\theta_{S,2}^{(k_c)})$ exhibits a complicated dependence on k_c. For

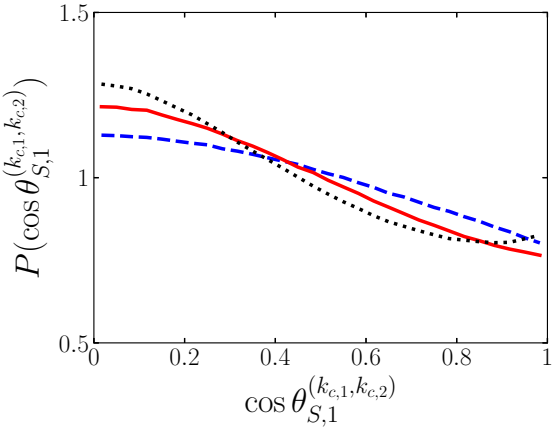

FIG. 15. PDF $P(\cos\theta_S^{(k_{c,1},k_{c,2})})$ of the cosine of the angle $\theta_S^{(k_{c,1},k_{c,2})} \in [0, \pi/2]$ between $\boldsymbol{e}_1^{(k_{c,1})}$ and $\boldsymbol{e}_1^{(k_{c,2})}$ of the bandpass-filtered strain-rate tensor at $\mathrm{Re}_\lambda = 220$ with forcing $\boldsymbol{f}^{(\mathrm{I})}$ for $k_{c,1} = k_c^*$ and $k_{c,2} = k_c^*/4$ (blue dashed), $k_c^*/2$ (red solid), and $2k_c^*$ (black dotted), where $k_c^* = 0.25k_\eta (= 64\sqrt{2}k_f/5)$.

$k_c = k_c^*$, which corresponds to the smallest scale in turbulence, $P(\cos\theta_{S,2}^{(k_c)})$ has the maximum value at $\cos\theta_{S,2}^{(k_c)} \simeq 0$, indicating that $\boldsymbol{e}_2$ and $\boldsymbol{e}_1^{(k_c)}$ at $k_c = k_c^*$ are orthogonal. However, for $k_c = k_c^*/4$, $P(\cos\theta_{S,2}^{(k_c)})$ has the maximum value at $\cos\theta_{S,2}^{(k_c)} \simeq 1$. This alignment indicates that the smallest-scale vortices tend to align with the most extensional direction induced by 4 times larger vortices than the smallest-scale vortices because it is well-known that the vorticity $\boldsymbol{\omega}$ preferentially aligns with $\boldsymbol{e}_2$ [44]. This observation is consistent with Ref. [45]. Next, we show the PDF $P(\cos\theta_S^{(k_{c,1},k_{c,2})})$ of the cosine of the angle $\theta_S^{(k_{c,1},k_{c,2})} \in [0, \pi/2]$ between $\boldsymbol{e}_1^{(k_{c,1})}$ and $\boldsymbol{e}_1^{(k_{c,2})}$ in Fig. 15. Here, to investigate the relationship between the smallest-scale vortices and other-scale vortices, we fix $k_{c,1}$ at k_c^* and change the value of $k_{c,2}$. Since $P(\cos\theta_S^{(k_{c,1},k_{c,2})})$ takes the maximum value at $\cos\theta_S^{(k_{c,1},k_{c,2})} \simeq 0$ irrespective of $k_{c,2}$ considered, the most extensional direction of the smallest-scale strain-rate fields tends to be orthogonal to that of other-scale strain-rate fields. However, we should note that the maximum value of $P(\cos\theta_S^{(k_{c,1},k_{c,2})})$ is not large partly because $P(\cos\theta_S^{(k_{c,1},k_{c,2})})$ is obtained without conditioning the turbulence intensity.

[1] A. Gyr and H.-W. Bewersdorff, *Drag Reduction of Turbulent Flows by Additives* (Kluwer Academic Publishers, Dordrecht, 1995).

[2] C. M. White and M. G. Mungal, Mechanics and prediction of turbulent drag reduction with polymer additives, Annu. Rev. Fluid Mech. **40**, 235 (2008).

[3] L. Xi, Turbulent drag reduction by polymer additives: Fundamentals and recent advances, Phys. Fluids **31**, 121302 (2019).

[4] E. D. Burger, W. R. Munk, and H. A. Wahl, Flow increase in the Trans Alaska Pipeline through use of a polymeric drag-reducing additive, J. Pet. Technol. **34**, 377 (1982).

[5] A. G. Fabula, Fire-fighting benefits of polymeric friction reduction, J. Basic Eng. **93**, 453 (1971).

[6] R. C. R. Figueredo and E. Sabadini, Firefighting foam stability: The effect of the drag reducer poly(ethylene) oxide, Colloids Surf. A **215**, 77 (2003).

[7] U. Frisch, *Turbulence: The Legacy of A. N. Kolmogorov* (Cambridge University Press, Cambridge, 1995).

[8] U. Frisch, P.-L. Sulem, and M. Nelkin, A simple dynamical model of intermittent fully developed turbulence, J. Fluid Mech. **87**, 719 (1978).

[9] P. Ilg, E. De Angelis, I. V. Karlin, C. M. Casciola, and S. Succi, Polymer dynamics in wall turbulent flow, Europhys. Lett. **58**, 616 (2002).

[10] P. A. Stone and M. D. Graham, Polymer dynamics in a model of the turbulent buffer layer, Phys. Fluids **15**, 1247 (2003).

[11] Q. Zhou and R. Akhavan, A comparison of FENE and FENE-P dumbbell and chain models in turbulent flow, J. Non-Newtonian Fluid Mech. **109**, 115 (2003).

[12] V. E. Terrapon, Y. Dubief, P. Moin, E. S. G. Shaqfeh, and S. K. Lele, Simulated polymer stretch in a turbulent flow using Brownian dynamics, J. Fluid Mech. **504**, 61 (2004).

[13] J. Davoudi and J. Schumacher, Stretching of polymers around the Kolmogorov scale in a turbulent shear flow, Phys. Fluids **18**, 025103 (2006).

[14] S. Jin and L. R. Collins, Dynamics of dissolved polymer chains in isotropic turbulence, New J. Phys. **9**, 360 (2007).

[15] T. Watanabe and T. Gotoh, Coil-stretch transition in an ensemble of polymers in isotropic turbulence, Phys. Rev. E **81**, 066301 (2010).

[16] S. Musacchio and D. Vincenzi, Deformation of a flexible polymer in a random flow with long correlation time, J. Fluid Mech. **670**, 326 (2011).

[17] J. R. Picardo, E. L. C. V. M. Plan, and D. Vincenzi, Polymers in turbulence: Stretching statistics and the role of extreme strain rate fluctuations, J. Fluid Mech. **969**, A24 (2023).

[18] J. L. Lumley, Drag reduction by additives, Annu. Rev. Fluid Mech. **1**, 367 (1969).

[19] J. L. Lumley, Drag reduction in turbulent flow by polymer additives, J. Polym. Sci. **7**, 263 (1973).

[20] M. Tabor and P. G. de Gennes, A cascade theory of drag reduction, Europhys. Lett. **2**, 519 (1986).

[21] H.-D. Xi, E. Bodenschatz, and H. Xu, Elastic energy flux by flexible polymers in fluid turbulence, Phys. Rev. Lett. **111**, 024501 (2013).
[22] P. C. Valente, C. B. da Silva, and F. T. Pinho, The effect of viscoelasticity on the turbulent kinetic energy cascade, J. Fluid Mech. **760**, 39 (2014).
[23] S. Goto and Y. Motoori, Hierarchy of coherent vortices in developed turbulence, Rev. Mod. Plasma Phys. **8**, 23 (2024).
[24] S. Goto, Y. Saito, and G. Kawahara, Hierarchy of antiparallel vortex tubes in spatially periodic turbulence at high Reynolds numbers, Phys. Rev. Fluids **2**, 064603 (2017).
[25] Y. Motoori and S. Goto, Generation mechanism of a hierarchy of vortices in a turbulent boundary layer, J. Fluid Mech. **865**, 1085 (2019).
[26] Y. Motoori and S. Goto, Hierarchy of coherent structures and real-space energy transfer in turbulent channel flow, J. Fluid Mech. **911**, A27 (2021).
[27] J. Fujino, Y. Motoori, and S. Goto, Hierarchy of coherent vortices in turbulence behind a cylinder, J. Fluid Mech. **975**, A13 (2023).
[28] T. Peters and J. Schumacher, Two-way coupling of finitely extensible nonlinear elastic dumbbells with a turbulent shear flow, Phys. Fluids **19**, 065109 (2007).
[29] T. Watanabe and T. Gotoh, Hybrid Eulerian-Lagrangian simulations for polymer-turbulence interactions, J. Fluid Mech. **717**, 535 (2013).
[30] T. Watanabe and T. Gotoh, Power-law spectra formed by stretching polymers in decaying isotropic turbulence, Phys. Fluids **26**, 035110 (2014).
[31] S. ur Rehman, J. Lee, and C. Lee, Effect of Weissenberg number on polymer-laden turbulence, Phys. Rev. Fluids **7**, 064303 (2022).
[32] F. Serafini, F. Battista, P. Gualtieri, and C. M. Casciola, Drag reduction in turbulent wall-bounded flows of realistic polymer solutions, Phys. Rev. Lett. **129**, 104502 (2022).
[33] P. Grassia and E. J. Hinch, Computer simulations of polymer chain relaxation via Brownian motion, J. Fluid Mech. **308**, 255 (1996).
[34] T. Uneyama, F. Nakai, and Y. Masubuchi, Effect of inertia on linear viscoelasticity of harmonic dumbbell model, Nihon Reoroji Gakkaishi **47**, 143 (2019).
[35] H. C. Öttinger, *Stochastic Processes in Polymeric Fluids: Tools and Examples for Developing Simulation Algorithms* (Springer, Berlin, 1996).
[36] A. G. Lamorgese, D. A. Caughey, and S. B. Pope, Direct numerical simulation of homogeneous turbulence with hyperviscosity, Phys. Fluids **17**, 015106 (2005).
[37] M. Hirota, Y. Nishio, S. Izawa, and Y. Fukunishi, Hierarchical vortical structures extracted from turbulent fields, Fluid Dyn. Res. **52**, 015503 (2020).
[38] P. G. de Gennes, Coil-stretch transition of dilute flexible polymers under ultrahigh velocity gradients, J. Chem. Phys. **60**, 5030 (1974).
[39] P. E. Dimotakis, The mixing transition in turbulent flows, J. Fluid Mech. **409**, 69 (2000).
[40] R. Ni, N. T. Ouellette, and G. A. Voth, Alignment of vorticity and rods with Lagrangian fluid stretching in turbulence, J. Fluid Mech. **743**, R3 (2014).
[41] S. Kida and S. Goto, Line statistics: Stretching rate of passive lines in turbulence, Phys. Fluids **14**, 352 (2002).
[42] Y.-B. Zhang, E. Bodenschatz, H. Xu, and H.-D. Xi, Experimental observation of the elastic range scaling in turbulent flow with polymer additives, Sci. Adv. **7**, eabd3525 (2021).
[43] M. E. Rosti, P. Perlekar, and D. Mitra, Large is different: Nonmonotonic behavior of elastic range scaling in polymeric turbulence at large Reynolds and Deborah numbers, Sci. Adv. **9**, eadd3831 (2023).
[44] W. T. Ashurst, A. R. Kerstein, R. M. Kerr, and C. H. Gibson, Alignment of vorticity and scalar gradient with strain rate in simulated Navier–Stokes turbulence, Phys. Fluids **30**, 2343 (1987).
[45] T. Leung, N. Swaminathan, and P. A. Davidson, Geometry and interaction of structures in homogeneous isotropic turbulence, J. Fluid Mech. **710**, 453 (2012).

Correction: During the proof cycle, Figures 12 and 15 were erroneously replaced by duplicate images of Figures 2 and 5. The correct images now appear for Figures 12 and 15.